Microstructure and hydrogen storage performance of ball-milled MgH_2 catalyzed by FeTi

MSc thesis

Roman Paramonov

Supervisor:

Dr. Révész Ádám, PhD. habil.

associate professor

Eötvös Loránd University,

Department of Materials Physics

Budapest 2022

Table of Content

Introduction

Continuous population development and growth lead to drastically increased energy consumption in the last decade. Most of modern energy sources are non-renewable and resulting in CO_2 or other greenhouse gases emission. Nevertheless, renewable energy sources attract more and more attention due to environmental reasons, global warming in particular. One of the renewable sources major downside is unpredictability, wind turbines can show maximal output at midnight, but they can stop at morning when consumption peak appears. Other significant problem is transportation, renewable sources usually geographically bonded to certain regions which can be remote relative to the consumption centers. Solution for these issues contains unavoidable energy storage step. One of the most promising energy storage solution is hydrogen. This molecular gas can be simply obtained from water by electrolysis and efficiently transformed back into water and energy by means of fuel cells without harmful by-products. There are three main storage forms for hydrogen: gas, liquid and solid. High pressure is needed to store a sufficient amount of hydrogen in gaseous form, liquid form provides a higher energy density but requires high energy input to reduce the temperature. Relatively low energy density and high explosion risks create barrier for production of mobile storage units. Solid phase storage provides enough energy density to compete with other modern energy storers and in addition it also prevents all the safety issues primarily caused by high pressure storage. There are two main routes for solid state hydrogen storage, both use host materials: adsorption and chemisorption based. The latter one can be considered as more perspective of the two since it possesses adjustable sorption-desorption parameters. In this case the best host material among all the elements is magnesium due to a maximal capacity of 7.6 wt.%. Various additives and modifications can be applied to adjust main parameters: kinetics, capacity, sorption/desorption temperature and pressure.

Literature review

1 Hydrogen

1.1 Hydrogen as an energy carrier

Hydrogen is the most abundant element in universe (75%), however on earth it is typically found in bonded state (H_2O, hydrocarbons etc.). Molecular hydrogen is non-toxic, highly volatile gas, its oxidation reaction is highly attractive exothermic reaction due water as the only by-product and relatively high produced energy due to unique electron per nucleon ratio which is the best among all elements (1) [1].

$$2H_{2(g)} + O_{2(g)} \rightarrow 2H_2O_{(l)} + 572\ kJ \quad (1)$$

1.1.1 Hydrogen economy

Hydrogen economy is a hypothetical term which incorporates a potential economy based on hydrogen utilization in transport, commercial, industrial, and residential sectors. Main idea of this economy is to partially replace fossil fuels introducing a green solution for global problems among which environmental pollution, depletion of fossil resources and climate change are the most substantial [2]. Hydrogen economy can be assembled from the seeing in Figure 1 steps:

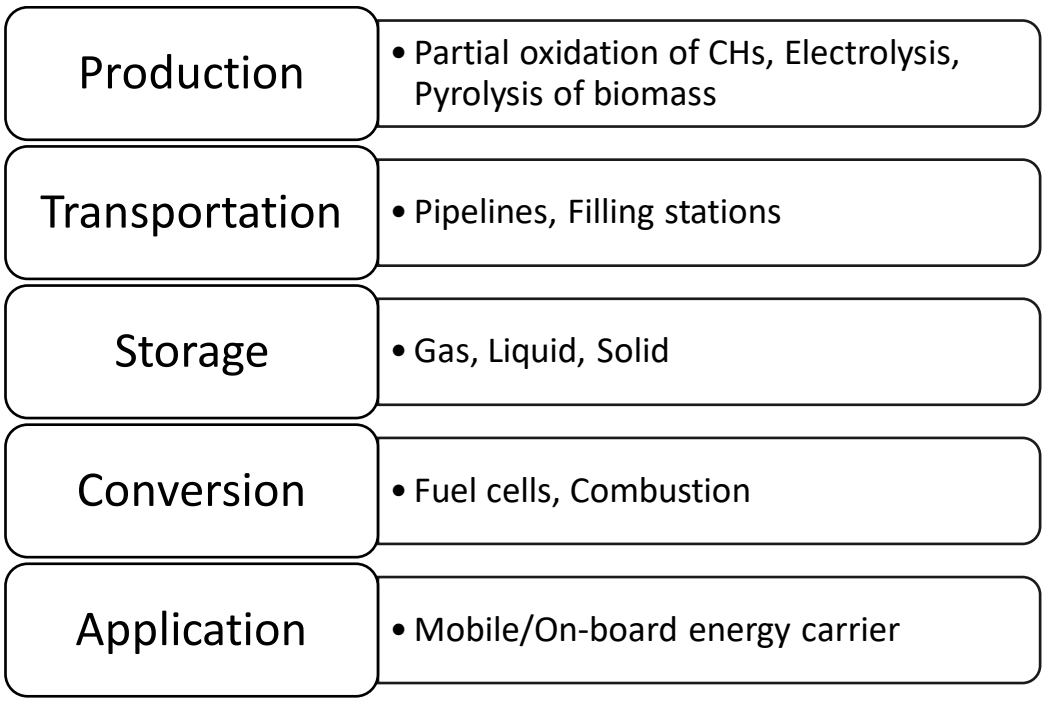

Figure 1. Hydrogen economy steps

Despite the fact that hydrogen utilization as an energy carrier has obvious advantages over the fossil fuels, it also faces significant scientific, technological and economical barriers. At the moment, cost of production, transportation, storage and delivery steps is too high for most applications [2].

Hydrogen storage is one of the most important aspects of this economy since it is essential for any mobile or on-board application. Even though hydrogen economy requires both, mobile/on-board and stationary systems to be developed, first ones are predicted to be much more popular in the future [2]. Detailed review on hydrogen storage topic is revealed in the following paragraph.

2 Hydrogen storage

2.1 Gaseous phase hydrogen storage

Gas state hydrogen storage implies application of vessels for gas storage with and without additional pressure. For an average car with a basic tank a normal petrol consumption is 24 kg for 400 km. To cover the same distance 4 kg of hydrogen is needed for an electric car or 8 kg for one with combustion engine. 4 kg of hydrogen occupies 45 m^2 at normal conditions which is competitive with totally inconvenient 5 m diameter tank. The most natural evolution of a hydrogen storage in a gaseous form is application of a pressure which can reduce volume of a gaseous body. There are few options of high-pressure tanks from cheap and affordable steel ones that can hold up to a 300 bar with optimal 200 bar to advanced composite ones which can withstand up to 700 bars with optimal 450 bar. High pressure also can be achieved by using simple aluminum spherical tanks wrapped with carbon fiber [3].

Four significant drawbacks follow high-pressure hydrogen storage techniques. First, fully loaded high-pressure tank contains only around 4 mass percent of hydrogen. Second, compressed flammable gases possess high explosion risks which makes such storage option undesirable for everyman usage. Third, the storage method itself requires an energy input which consumes up to 20% of stored amount. Fourth, frequent filling/discharging cycles cause brittleness of tank materials significantly reducing container's lifespan [3, 4].

2.2 Liquid phase hydrogen storage

Liquid hydrogen possesses much higher density, drastically improving mass per volume ratio for a fuel tank comparing with the gas phase storage. On the other hand, to initiate gas-liquid transformation for hydrogen a -241°C cryogenic temperature must be achieved with addition of a high pressure, that requires large amount of energy. After liquefaction hydrogen has tendency to evaporate (boil-off) which can lead up to a 40% fuel loss directly resulting in economical and safety problems. Issues listed before and mostly extreme conditions of liquid hydrogen containment represent discussed storage approach as poorly applicable for a common usage such as fuel for a personal car [3, 4].

2.3 Solid phase hydrogen storage

Two conventional storage methods discussed above have unresolved problems such as lack of safety for gas phase storage and evaporation for liquid phase storage. Application of solid materials as hosts for hydrogen containment is an option that completely overcomes these weaknesses. There are 2 distinct mechanisms based on which these materials can store hydrogen. Adsorption mechanism is used in microporous minerals (zeolites), metal-organic framework systems (MOFs) and various carbons structures where hydrogen molecules are connected to the host material by Wan-der-Waals forces. Absorption or chemisorption is related to utilizing of metals to chemically bind atomic hydrogen forming metal hydrides [4].

2.3.1 Adsorption based hydrogen storage materials

Adsorption or physisorption mechanism implies presence of a large surface area like in zeolites, microporous aluminosilicate minerals which are typically used in catalyst and gas separation processes such as adsorption of undesirable compounds from natural gas stream. These minerals possess well defined and adjustable open-pore structure which supposed to keep hydrogen. The network structure of zeolites usually consists of AlO_4 and SiO_4 species with diverse space arrangement [5]. Zeolites are promising candidates for hydrogen storage due to their tunable composition, low cost, high thermal and structural stability. Hydrogen storage capability of several zeolites was studied at cryogenic temperature (77K) [6, 7], the largest stored amount of 2.07 wt.% was achieved for Na-LEV (levyne – hydrated silicate mineral). Other papers investigated hydrogen storage capacity for various zeolites at different pressure and non-cryogenic temperature resulting maximal hydrogen uptake occurred to be not higher than 0.4 wt.% [8, 9]. Although being promising hydrogen storage materials, zeolites require further investigations mainly in order to increase maximal capacity since this parameter is still below potential of other promising adsorbents [4].

MOFs are new nonporous materials which consist of organic ligands coordinated via metal ions or clusters forming one-, two- or three-dimensional systems. MOFs are considered superior to zeolites in many aspects such as larger surface area and variability. Pore size of these materials is controlled by the length of carbon chain linkers and number of benzene rings in them. Addition of various functional groups to the linker can reveal selectivity and other chemical properties of the pores. These properties make MOFs a promising material class for hydrogen storage application [10, 11].

Two reports [12, 13] provided experimental results on hydrogen uptake of MOF-177 and PCN-61 (porous coordination network) at 77K which showed 7.5 wt.% under 70 bar and 6.24 wt.% under 35 bar, respectively. A potential development direction of MOFs can be represented by various calculations. Results of theoretical calculations for MOFs and covalent organic framework systems (COFs) (similar to MOFs but coordinated not via metal ions but via strong covalent bonds) were revealed in order to find structure that can show maximal possible hydrogen uptake [14]. It occurred that the COF-105 able to adsorb up to 21 wt.% hydrogen at 77 K and 100 bar and 4.5 wt.% at room temperature and 100 bars. Another group calculated hydrogen delivery uptake for similar COFs and MOFs metallized with Li, Na and K at room temperature and 1-100 bar range, results have sown that Li metalized MOF200-Li (6.34 wt.%), COF102-Li (5.16 wt.%) and N-metalized MOF200-Na (5.94 wt.%), COF102-Na (4.75 wt.%) provide best uptake behavior and maximal values at a given range [15]. It should be mentioned that previously described results are related to calculations which supposed to investigate a plausibility for manufacturing of such materials while currently achieved practical results show sufficient uptake only at cryogenic temperatures. In addition, despite being one of the most promising materials for hydrogen storage COFs and MOFs production is still rather expensive and complicated process [16].

Carbon nanostructures also possess potential to store hydrogen by means of adsorption. Main features of these materials are light weight, enormous surface area and high chemical stability [4]. Several papers focused on pure carbon nanotubes (CNTs) adsorption of hydrogen [17-19], reported that single walled nanotubes (SWCNTs), even being superior to multi walled carbon nanotubes, (MWCNTs) in area of hydrogen storage, have experimental capacity limitation of 0.5 wt.% at room temperature in 1-100 bars range which is not even close to the U.S. Department of Energy goal of 6.5 wt.%. The main reason of such low performance is insufficient Wan-der-Waals force between hydrogen molecules and tube walls and consequentially low binding energy [20]. Direct solution of the pointed problem can be achieved by doping/functionalization of CNTs. Couple of recent papers provided computation results for modified CNTs hydrogen storage capacity at room temperatures, the first group concluded that hemisphere sections of capped CNTs doped by Sc can store up to 7.08 wt.% [21], second group revealed a theoretical estimations of Li doped CNTs ability to store more than 10 wt.% of hydrogen [22]. As well as in the case of MOFs, recent calculations for modified CNTs provide only a potential investigation direction since production route for most of previously mentioned materials is still unclear or too impractical.

2.3.2 Chemisorption based hydrogen storage materials

Absorption mechanism utilized for hydrogen storage is typically related to various hydrides. These materials can be divided into 3 groups: metal hydrides, complex hydrides, and chemical hydrides. Despite the fact that their common feature is superior, comparing to adsorption type materials, capacity at normal conditions, hydrides yet possess tangible problems with reversibility and activation energy [23, 24].

2.3.2.1 Chemisorption kinetics

Figure 2 depicts the absorption sequence for some metallic hydrogen storage material (E.g. MgH_2). In general, this process can be divided into 4 steps:

1) Dissociation and adsorption: First, hydrogen molecules are adsorbed weakly by Wan-der-Waals forces on the surface of metal, after that these adsorbed molecules undergo dissociation so that each molecule transforms into 2 hydrogen atoms.
2) Surface penetration: Hydrogen atoms start to penetrate into the sub-surface layer.
3) Bulk diffusion: Hydrogen starts to diffuse into the bulk forming solid solution (α).
4) Hydride formation: After reaching critical local concentration hydrogen atoms form a hydride nucleus which grows by trapping additional hydrogen atoms up to a larger hydride grain resulting in a hydride phase (β).

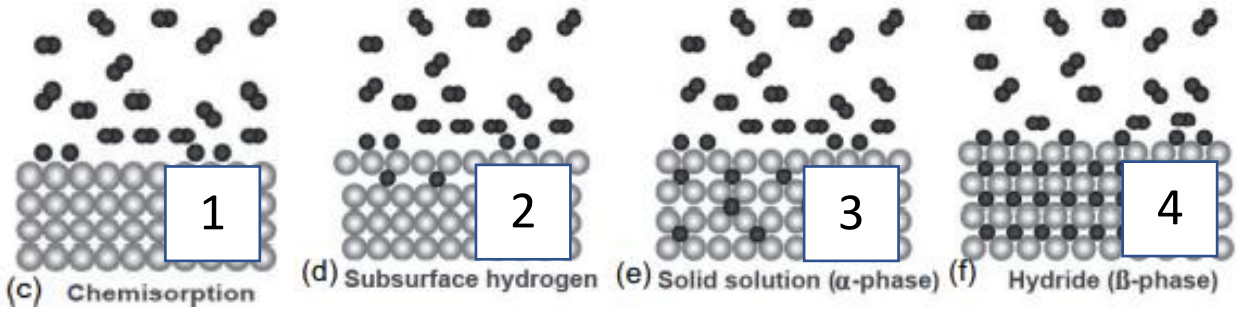

Figure 2. Schematic illustration of hydrogen absorption mechanism for metals [25]

Hydrogen desorption is the reverse of this process, i.e. hydrogen atoms diffuse from the bulk into sub-surface level from which they reach the surface ad recombine into H_2 molecules [25].

2.3.2.2 Kinetic modelling for chemisorption

The slowest step (rate-limiting) among listed in the Paragraph 2.3.2.1 determines kinetics of the absorption/desorption process [25]. Modelling is essential part of sorption mechanisms characterisation. There are various models which take into consideration different rate-limiting steps. The most known among them are: Single-particle reacted model (SC) [26] Johnson-Mehl-Avrami model (JMA) [27-29] and contracting volume (CV) model [29].

1) SC model. This model takes into consideration dissociation of molecules during absorption and recombination of H_2 molecules during desorption as a rate-limiting step. Reacted fraction α is proportional to the sorption time t (Fig. 3 a):

$$a(t) = kt\ , \tag{2}$$

where k – temperature dependent reaction rate [25, 26].

2) JMA model. This model describes sorption process as nucleation of second phase randomly distributed particles on the surface or in the bulk (3). Shape of the α(t) expression (3 a) follows S-like sorption curves (Fig. 3 c).

$$\alpha(t) = 1 - e^{-kt^n} \quad \text{or} \tag{3 a}$$

$$[-\ln(1-\alpha)]^{\frac{1}{n}} = kt, \tag{3 b}$$

where k – depends on temperature, n – determines growth dimensionality of a new phase. Rate limiting step in this case is moving interface (metal hydride/metal) with assumption that diffusion is fast enough [27-29].

3) CV model. Unlike JMA, CV model considers that nucleation and growth of a second phase start predominantly from the surface propagating into the bulk. If the diffusion is not the rate-limiting step (diffusion is fast enough) and interface propagates with constant velocity the kinetic equation can be expressed as (4) see also (Fig. 3 b):

$$\alpha(t) = 1 - (1-kt)^n \quad \text{or} \tag{4 a}$$

$$1 - [1 - \alpha]^{\frac{1}{n}} = kt, \quad (4\text{ b})$$

where (n) can take values n = 2 or n = 3 for two- and three-dimensional growth of a given nuclei, respectively. If diffusion is a rate-limiting step so that interface moves with decreasing velocity kinetics can be described as [29]:

$$1 - \left(\frac{2\alpha}{3}\right) - (1 - \alpha)^{\frac{2}{3}} = kt \quad (5)$$

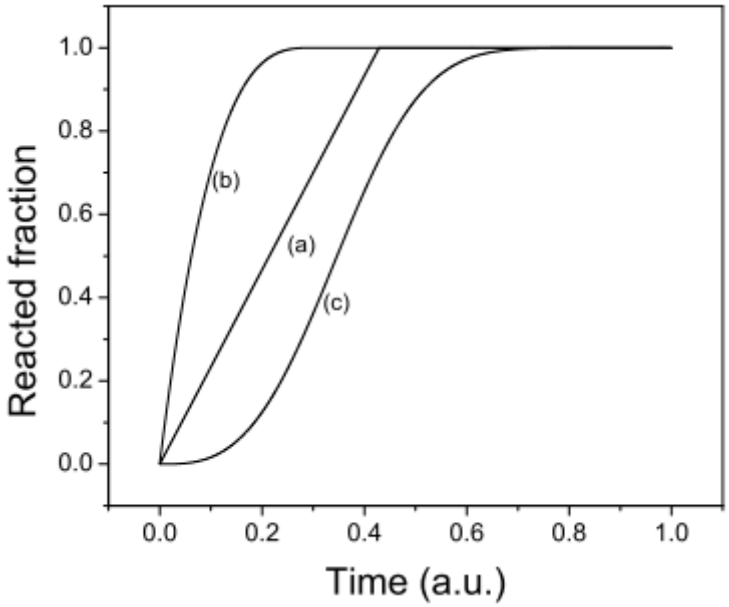

Figure 3. SC model type (a), CV model type (b), JMA model type (c) sorption a(t) function curves [30]

2.3.2.3 Chemisorption thermodynamics

Thermodynamic aspects of the hydride formation for a typical intermetallic compound or metal (including Mg) are shown in the Figure 4, where α-phase denotes the solid solution of hydrogen in the metal phase, β-phase is the hydride phase. Coordinate axes compare pressure (bar) and concentration in (H/M) aka hydrogen per metal atom. At low concentrations (below 0.1 H/M) hydrogen can only occupy interstitial position with formation of a solid solution, this step coincides with rapid pressure growth. At a critical concentration a phase transformation at a constant pressure takes place, this pressure strictly depends on temperature. The co-existence of two phases vanishes above the critical temperature (T_c), above which the α→β transition is continuous. Equilibrium pressure ρ_{eq} at which the phase transformation takes place can be related

to the changes of enthalpy (ΔH) and entropy (ΔS) of a hydride formation through the temperature. This relation can be expressed through the Van't Hoff equation:

$$\ln\left(\frac{\rho_{eq}}{\rho_{eq}^{0}}\right) = \frac{\Delta H}{R} \cdot \frac{1}{T} - \frac{\Delta S}{R}, \tag{6}$$

where ρ_{eq}^{0} is a reference pressure (typically, atmospheric pressure) [24].

Van't Hoff plot (Fig. 4, right) provides ΔH and ΔS from the slope and the intersect of the fitted line. Since the entropy change corresponds to the transformation of the molecular hydrogen gas into dissolved (in some matrix) solid hydrogen, it can be approximated by the standard value for hydrogen ($\Delta S = S_0 = 130\ J \cdot K^{-1} mol^{-1} H$). Enthalpy in opposite characterizes the stability of metal hydrogen bond, consequently it depends on which metal forming the hydride and directly affects sorption performance of a given material [24, 31].

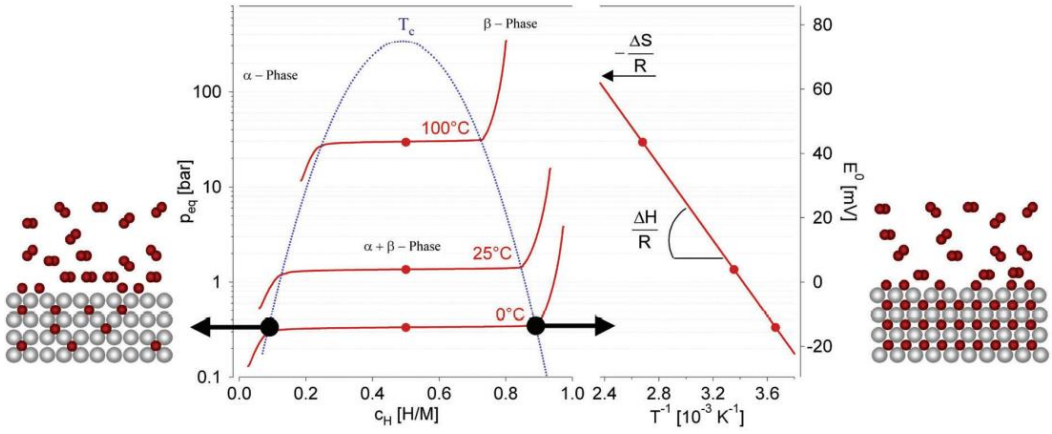

Figure 4. Pressure composition isotherms for the typical metallic or intermetallic compound capable to store hydrogen (left side). Van't Hoff plot (right side) [31]

2.3.2.4 Complex hydrides

Main advantage of complex hydrides are the light elements composing them. That provides remarkable for such materials gravimetric energy density. Alanates are complex aluminum hydrates mostly featured for relatively high potential hydrogen capacity (more than 10 wt.%) and unusual hydrogen release process, through the contact with water and subsequent chemical reaction (7, 8) [23]. Noticeable material in this group is sodium alanate with formula $NaAlH_4$ its achieved reversible storage capacity is 5.6 wt% in addition this hydride is cheap and can be easily obtained in a bulk form. The main downside of the sodium alanate is two step dehydrogenation reaction with different released amounts of hydrogen 3.70 wt.% for the first and 1.85 wt.% for the second step.

$$NaAlH_4 \leftrightarrow \frac{1}{3}Na_3AlH_6 + \frac{2}{3}Al + H_2 \quad (7)$$

$$Na_3AlH_6 \leftrightarrow NaH + Al + \frac{3}{2}H_2 \quad (8)$$

This detail results in a slow kinetics, harsh conditions of dehydrogenation and bad reversibility. Application of a various catalysts such as $TiCl_3$ or TiF_3 compounds and doping of the material with Ti by addition of $Ti(OBu)_4$ catalyst during milling of complex hydride starting materials (Al and NaH) provides a significant improvement of kinetics and cyclic life by reducing maximal reversible storage capacity. There is another interesting materials class in the mentioned group, borohydrides or more precisely tetrahydroboates are considered as the highest hydrogen capacity storage compounds with additional ability to safely dissolve in water. The decomposition process of these materials is somewhat different comparing to alanates, without intermediate hexahydride as it shown in (9) and (10) [23, 32].

$$M(BH_4)n \rightarrow nMH + nB + \frac{3}{2}H_2 \quad (9)$$

$$nMH + nB \rightarrow nB + nM + \frac{1}{2}H_2 \quad (10)$$

$LiBH_4$, $NaBH_4$, $Mg(BH_4)_2$ and $Ca(BH_4)_2$ possess a great potential as a hydrogen storage materials, in particular it was shown [31] that $LiBH_4$ has total 18.5 w.t% hydrogen capacity, however the best achieved reversible amount is 13.5 wt.% for SiO_2 catalyst sample, the reason of such limitation is thermodynamically stable up to 1173 K lithium hydrate (LiH). In general, despite having the best capacity hydroborates also possess severe issues such as high thermodynamic stability, short cyclic life and relatively poor kinetics which makes these materials inapplicable for reversible hydrogen storage application [33].

2.3.2.5 Chemical hydrides

Chemical hydrides consist of a lighter element comparing to metal hydrides, resulting in relatively high gravimetric hydrogen storage capacities. Considering given researches [34-36], ammonia borane (NH_3BH_3) drew a particular attention due to gravimetric storage potential of 19.5 wt.% and stability in basic and neutral aqueous solutions. For this material hydrogen evolution is a 3-step exothermic process [37]. Few major downsides make this material yet inapplicable as a mobile storage unit among which fast hydrolysis in acids, complicated synthesis process, formation of concomitant B_2H_6 poisonous impurities and sluggish kinetics at normal conditions. There are various potential solutions of the raised problems, addition of lithium hydride (LiH) and lithium nitride $LiNH_2$ can significantly improve kinetics while ball milling of ammonia borane

with lithium hydride (LiH) results in a lithium amidoborane ($LiNH_2BH_3$) which does not release poisonous B_2H_6 compound [23].

2.3.2.6 Intermetallic and metal hydrides

Metal hydrides and intermetallic compounds capable to absorb hydrogen received noticeable attention due to their ability to store sufficient amount of hydrogen, appropriate cyclic life and highly tuneable sorption/desorption parameters [23, 24]. Hydrogen storage properties of intermetallic compounds strictly depend on interaction of an interstitial hydrogen atom with host atoms consequently properties directly related to the lattice structure of the material. Having a common formula of $A_nB_mH_x$ intermetallic hydrogen storage compounds can be divided into several lattice groups: AB_5, AB_2, AB, A_2B.

AB_5 group popularity in hydrogen storage researches relates to compounds composed of rare earth metals and d-metals. One of the most representative members of this group is $CaCu_5$ based hexagonal structures due to the highest discharge capacity (among AB_5 members), relatively fast kinetics, good cyclic life, low cost, and low equilibrium pressure. The main drawback of this material is limited theoretical storage capacity around 1.5 wt.% with real discharge capacity being even lower [23, 38]. Similar properties description can be given to $LaNi_5$ systems except even faster kinetics at the expense of a higher cost. Vexing hydrogen storage capacity limitation of 1.5 wt.% and released capacity of 0.9 wt.% for this material may be overcome by partial substitution of La and Ni. For example, Al substitution of Ni resulting in $LaNi_{4.5}Al_{0.5}$ composition significantly reduces activation energy and increases hydrogen discharge amount. Overall, the U.S. Department of Energy goal of 6.5 wt.% seems unachievable at the moment [39, 40].

Low molar mass and high capacities per weight are distinctive features of AB – intermetallic structures make them interesting for potential hydrogen storage applications. Leading role in this group is related to the FeTi based intermetallic compounds with cubic CsCl-type structure which allow formation of $FeTiH_2$ hydride. These compounds able to reversibly absorb up to 1.9 wt.% of hydrogen and considered as a relatively cheap alternative to the expensive systems like $LaNi_5$. On the other hand, FeTi systems have sluggish kinetics, high equilibrium temperature and yet low capacity which cannot match previously mentioned U.S. Department of Energy goal. Potential substitution option for TiFe compound that can improve cyclic life is Fe substitution by a similar element – Ni [41]. Full Fe substitution is also acceptable, TiNi system still has hydrogen absorption capability but with lower values (up to 1.2 wt.%), also an absorption reaction can be

hindered upon formation of a surface oxide. In this case partial substitution of Fe in TiFe seems more beneficial since Mn, Ni, Cr, and V facilitate activation and reduce equilibrium pressure [42].

AB_2 intermetallic compounds or Laves-phases capable to store hydrogen typically represented by A - Ti (Titanium) or Zr (Zirconium) and B – transition metals. The most crucial problem of such materials is high cost of transition metals [43]. Hydrogen storage properties of $ZrFe_{1.8}M_{0.2}$ intermetallic compounds where (M = V, Cr, Mn, Fe, Co, Ni, Cu, Mo) were investigated, subsequent storage capacity was maximal for V containing alloy 1.8 wt.% and lowest for Mo containing 1.6 wt.% [44]. Some results were revealed regarding hydrogen storage properties of a complex AB_2 alloy $Zr_{21.5}V_{10}Cr_{7.5}Mn_{8.1}Co_{8.0}Ni_{32.2}Sn_{0.3}Al_{0.4}$ where Co content was also substituted with Y (yttrium). The maximal reversible amount of hydrogen at 333 K was obtained for Y containing alloy 1.36 wt.% at a pressure of 0.056 MPa [45].

There are various metal hydrides with feasible potential of energy carrier application, for example $PdH_{0.6}$, rare earth REH_3, REH_2 and MgH_2 but none of them satisfy appropriate for mobile storage sorption/desorption conditions (1-100 bar, 273-373 K). However, there are various techniques and additives which can create a potential of mobile application for some of them. Among all metal hydrides magnesium-based systems have gained the closest attention due to especially high gravimetric 7.6 wt.% and volumetric 0.11 kg H/l capacities. As an additional advantage magnesium is a lightweight, non-toxic, abundant and relatively cheap (in terms of production) material [3, 24, 46]. A more detailed description on magnesium as a hydrogen storage material is presented in the next chapter.

3 Magnesium based hydrogen storage materials

3.1 Hydrogen storage properties of MgH_2

As it was mentioned, magnesium has high gravimetric (7.6 wt.%) and volumetric (0.11 kg H/l) capacity, while it is lightweight, non-toxic, abundant, and cheap. Mg can absorb and desorb hydrogen reversibly according to:

$$Mg(s) + H_2(g) \rightarrow MgH_2(s). \quad (11)$$

The thermodynamic calculations for Mg-H system resulting in phase diagrams at different pressures can be seen in the Figure 5 [47]. It clearly shows that hydride formation takes place at 560.7 K. This low-pressure hydride possesses tetragonal TiO_2 (rutile type) unit cell with a space group of $P4_2/mnm$ it also can be referred as α-MgH_2. Mg-H interaction in this polymorph form of the hydride is complex, mostly ionic, but with presence of a covalent part. At high pressure values (above 8 GPa) a polymorphic transformation takes place resulting in the formation of the γ-MgH_2 phase with orthorhombic unit cell (PbO_2 structure) [48, 49].

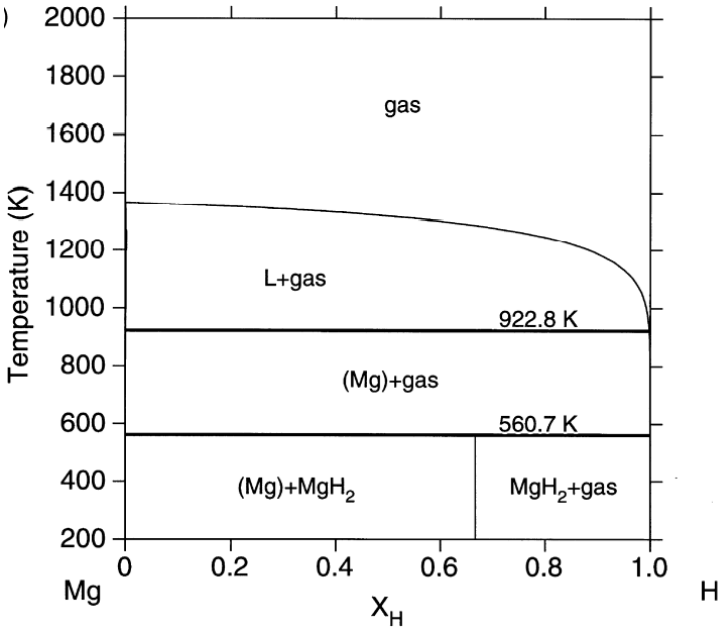

Figure 5. Calculated Mg-H phase diagram at 1 bar [47]

Some conclusions were made regarding Mg thermodynamics, i.e. -39 kJ mol^{-1}H are needed to reach ρ_{eq} at 1 bar according to the equation (6) [24] while enthalpy of formation for tetragonal MgH_2 is significantly higher (ΔH = -74.5 kJ mol^{-1}H) [50]. Such gap suggests that equilibrium hydrogenation/dehydrogenation state can be reached only at elevated temperatures. For example, it is concluded that to desorb hydrogen at p = 1 bar magnesium hydride should be heated up to 550

K [50]. If the pressure is around 10 bar, then the desorption temperature is 640 K as confirmed by Figure 6.

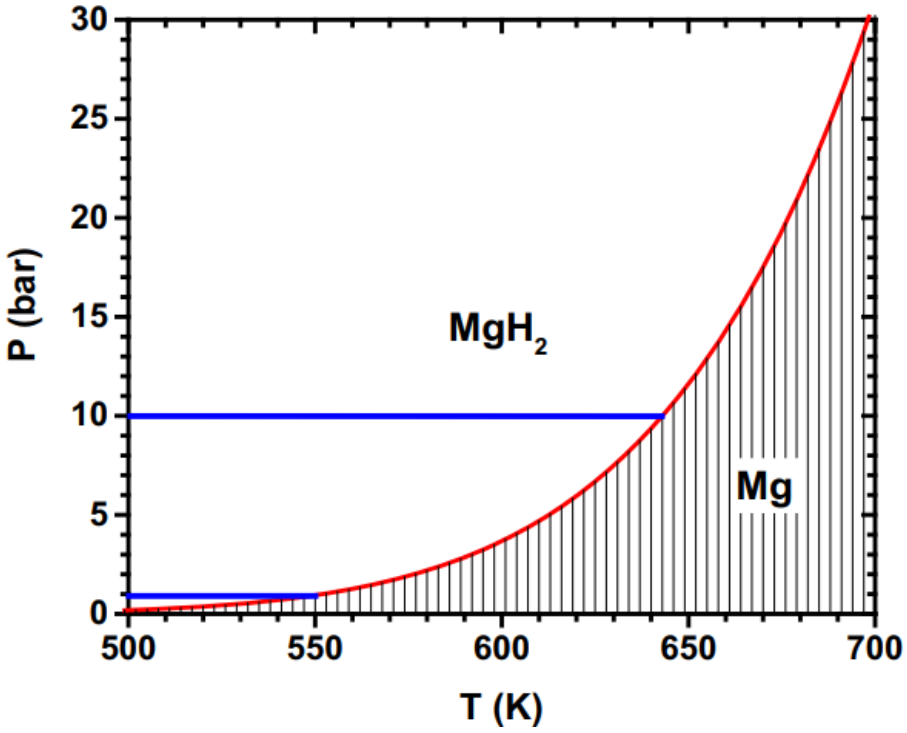

Figure 6. Temperature dependence of the MgH_2 dissociation pressure [50]

Magnesium related activation energy for hydrogen absorption and desorption can be considered as high: E_{act}^{abs} = 90 kJ/molH and E_{act}^{des} = 152-180 kJ/molH, respectively [51]. As a conclusion, pure magnesium possesses poor kinetics at ambient temperatures as a result of thermodynamic aspects described above. Such downsides apply serious limitations for the on board/mobile application of Mg as a host storage material.

There are two main solution routes in order to overcome the thermodynamic and kinetics barriers of MgH_2. First, it is a grain refinement or reducing of the grain size down to nanometres scale. Several papers investigated this effect [52, 53], however, a general point is that significant reduction in the enthalpy of the hydride formation can be observed for clusters containing around 10 magnesium atoms, realistically, barely achievable value [54]. Nevertheless, crystalline size refinement with consequent surface area growth and inducing of various defects (mainly dislocations and vacancies) can directly affect sorption kinetics promoting hydrogen diffusion along the grain boundaries and lattice defects [55, 56].

Another solution to improve the kinetics of magnesium is alloying, or introduction of other catalyst can significantly reduce ΔH. One of the most investigated routes is application of Ni, resulting in a formation of Mg_2Ni phase and corresponding hydride, consequently, the reduction

of the formation enthalpy to ΔH = -64.5 kJ $mol^{-1}H_2$ [57, 58]. Critical downside of such alloying is concomitant reduction of the maximal capacity (3.6 w.t%). General development vector in this area is inclined towards simultaneous application of a grain refinement (for example, by ball milling) and various additives including alloying elements and different nanoparticles such as oxide nanoparticles or carbon nanostructures [24].

3.2.1 Effect of grain refinement on Mg hydrogen sorption properties

According to the research dedicated to effect of grain refinement on Mg hydrogen sorption properties, it was concluded that extensive ball milling greatly improves sorption kinetics of catalyzed MgH_2 due to nano-crystallization effect [59]. A deep review regarding lattice defect effects on sorption performance of catalyzed Mg was conducted [60]. It was concluded that previously mentioned improvement of sorption performance results from surface defects (substitutional atoms) which play a major role in hydrogen dissociation and various kinds of defects through all the sample volume mainly grain boundaries and dislocations along which hydrogen can easily diffuse. It should be mentioned that ball milling procedure not only affects the structure of a host material but also works for even distribution of catalyst particles and surface layer solid state alloying. It was also pointed that extreme deformation degrees achieved by equal channel angular pressing technique could significantly improve hydrogen sorption performance even for non-catalyzed Mg. Positive effect of grain refinement on kinetics was also supported by theoretical calculations, analytical model successfully provided hydrogen diffusion coefficients for hydrogen diffusion in Mg related to different crystallite sizes and temperatures [61].

Special attention should be given to structure evolution of nano-crystalized MgH_2 during absorption/desorption cycles. Significant crystallite size increase from 20 nm to 86 nm can be achieved for Mg after 2000 cycles of hydrogenation/dehydrogenation [62]. It was also proved that grain size inhomogeneity increases with increasing number of sorption cycles for nano crystallized Mg, the reason of such effect is in initially large grains which preserve residual MgH_2 inclusions because of short active desorption period. These inclusions eventually result in an inhomogeneous microstructure since, newly formed on the surface, hydride front can no longer occupy whole grain [55] (Fig. 7).

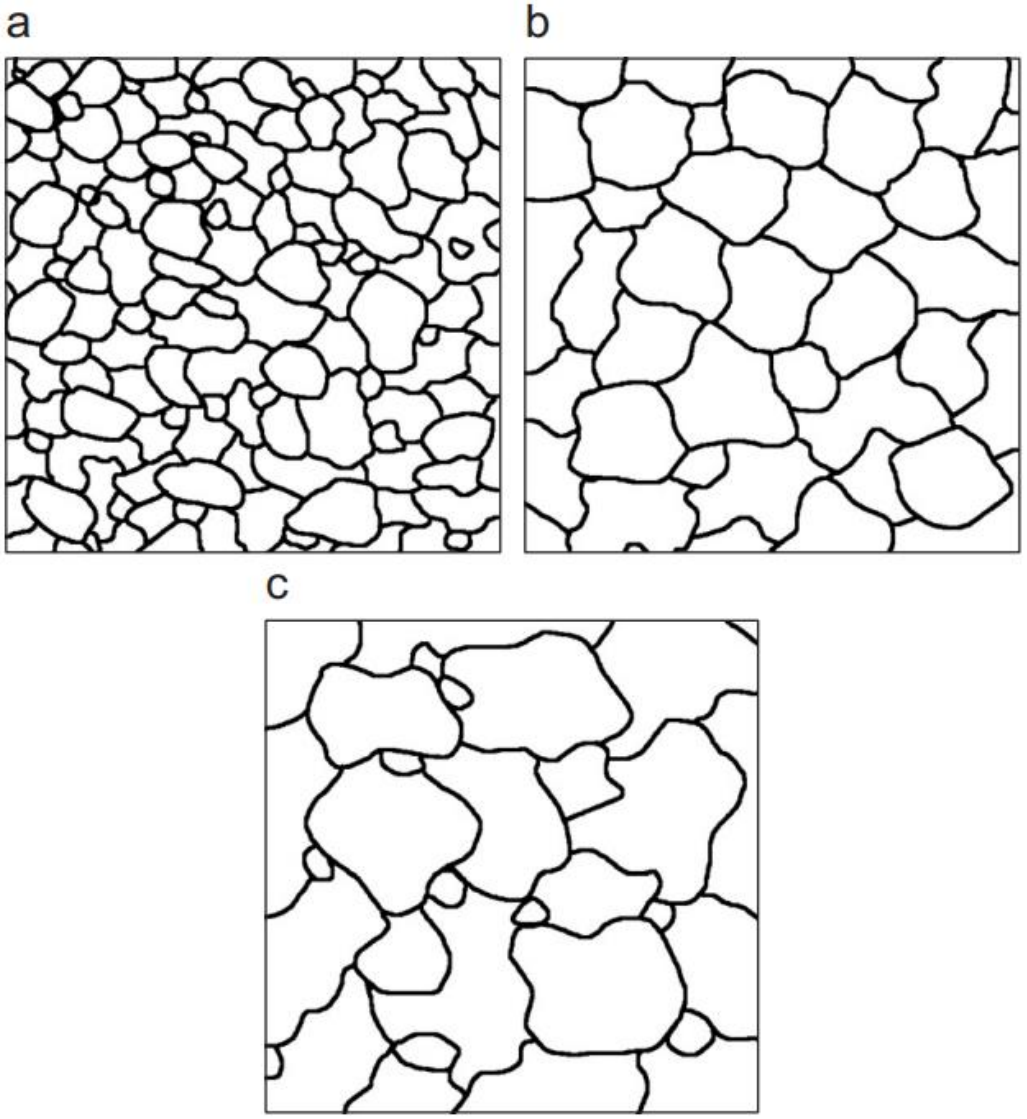

Figure 7. Initial microstructure (a), microstructure after 1 hydrogenation/dehydrogenation cycle (b), microstructure after several cycles (c).

Effect of grain refinement directly on hydride formation enthalpy and sorption temperature consequentially, was previously mentioned in Paragraph 3.1. Significant effect on ΔH can be achieved only for 10 Mg atom clusters [54]. Nevertheless, in a specific cases high energy ball milling may lead to formation of previously mentioned metastable γ-MgH_2 phase which by destabilization Mg-H bond significantly reduces sorption temperature [63].

3.2.2 Effect of catalyst on Mg hydrogen storage properties

There are various additives which can be used to improve kinetics, equilibrium conditions and cyclic life of magnesium hydride. Transition metals, metal oxides, intermetallic compounds,

in-situ formed catalysts, various nanostructures (including carbon nanotubes and graphene) and their synergetic combinations are often featured in MgH_2 related literature [24].

3.2.2.1 Transition metals and their oxides as MgH_2 catalysts

One of the main catalyst in this area is Ni which is proven to have positive effect on hydrogen storage properties of Mg/MgH_2 due to reduction of ΔH. Mg and Ni interaction results in a formation of intermetallic compound Mg_2Ni capable to store hydrogen [64]. High energy ball milling (HEBM) technique utilized for mixture of Mg and Ni powder can result in a formation of Mg_2Ni compound due to a solid-state alloying. Such material has significantly lower dehydrogenization temperature comparing to the pure MgH_2 [65]. Hydrogenated state of Mg_2Ni compound is characterized by the hexagonal $Mg_2NiH_{0.3}$ for solid solution and triclinic Mg_2NiH_4 for the final hydride phase [65]. Enthalpy change for nanocrystalline Mg_2Ni – Mg_2NiH_4 significantly lower than such for non-catalyzed magnesium and slightly lower than for coarse grained Mg_2Ni (ΔH = -57.47 kJ $mol^{-1}H_2$ for nano-crystalized Mg_2Ni comparing to ΔH = -74.5 kJ $mol^{-1}H_2$ for non-catalyzed Mg comparing to ΔH = -64.5 kJ $mol^{-1}H_2$ for coarse grained Mg_2Ni) [64]. By the proper synthesis optimisation of Ni modified MgH_2 it is possible to obtain fully transformed γ-MgH_2 sample with ability to desorb 4.3 wt.% of hydrogen at 200 °C [66]. Further improvements regarding desorption temperature can be done by application of various Ni – based catalyst such as Ni_3C, Ni_3N, NiO and Ni_2P. The lowest dehydrogenation temperature among these materials was achieved for Ni_3C-MgH_2 composite (160 °C) [67].

Nanocrystalline Fe is another promising catalyst material for Mg with even stronger effect, comparing to Ni, on temperature of hydrogenation which can be reduced down to 273 K with 45 % of theoretical capacity at moderate pressures [68]. When Mg powder was milled with Fe powder in a high energy planetary ball mill, the samples after hydrogenation contained not only MgH_2 and Fe particles but also Mg_2FeH_6 compound fraction of which increases with increase milling time. It was concluded that mostly distributed Fe nanoparticles are responsible for a substantial kinetics improvement while Mg_2FeH_6 complex hydride slightly increases desorption temperature and reduces reversible capacity at lower temperatures (300 °C) therefore formation of the complex hydride results in a negative effect on a hydrogen storage properties of Mg-Fe powder composite. Iron oxide (III) – Fe_2O_3 also bears a significant catalytic effect on MgH_2 performance [69]. When Ball milled MgH_2 with 10 wt.% of Fe_2O_3 catalyst was prepared, a significant kinetics acceleration effect of the oxide particles was revealed [70]. Also, it was shown that the rate limiting step of

hydrogeneration is hydrogen dissociation at the surface of Mg based on behaviour of Fe_2O_3 catalysed Mg [71].

TiO_2 also can be considered as one of the best catalyst materials for Mg since it significantly improves hydrogenation/dehydrogenation properties of magnesium especially reduction of the desorption temperature [24]. Recent research also revealed evidence of TiO_2 particles size and morphology correlation with H-storage properties of Mg [72]. When TiO_2 particles were added with various proportion of {001} and {101} facets to Mg, it was shown that a TiO_2 catalysed sample with prevailing {001} facets has the lowest hydrogen desorption temperature and fastest kinetics (Fig. 8) [73]. Other team provided exact desorption activation energy values for TiO_2 plates doped Mg, after addition of the catalyst desorption activation energy was reduced from 186.78 kJ mol^{-1} (undoped Mg) to 67.64 kJ mol^{-1} [74].

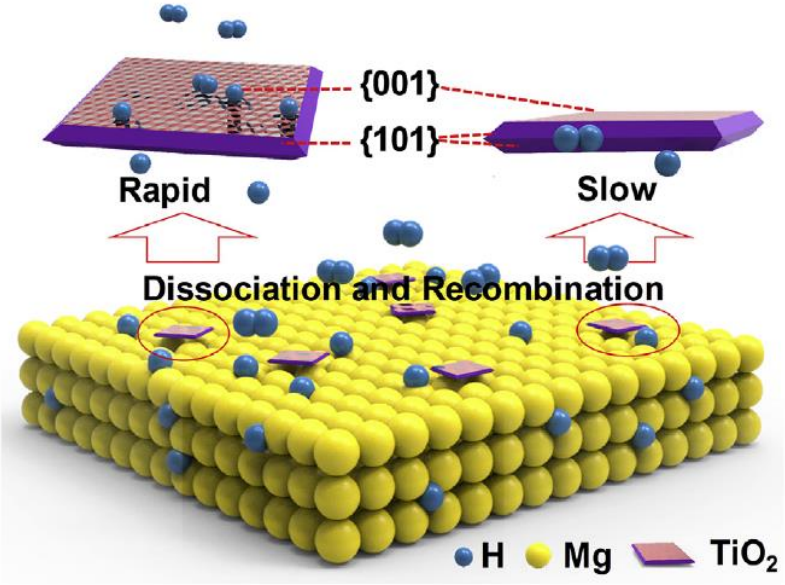

Figure 8. Schematic illustration of hydrogen dissociation and recombination on the surface of TiO_2 sheets [73]

3.2.2.2 Intermetallic compounds

Intermetallic compounds as a catalyst for Mg receive increasing popularity nowadays. When Mg-40%FeTi mixture was milled by HEBM technique with different parameters (such as milling time and rpm), it was found that FeTi catalyst has an effect on the absorption properties of Mg at room temperature (RT), results revealed that addition of the intermetallic compound significantly improved hydrogen absorption kinetics [75]. It was also shown that pre-milling and additional refinement of FeTi is beneficial for storage capacity. Similar research revealed that

longer milling process in a planetary ball mill results in a sample with better kinetics (3 wt.% absorbed after 60 min), when Mg was milled with 40, 50 and 60 wt.% of FeTi, however the highest maximal capacity was achieved for the sample which was milled with higher intensity and shorter milling time in a shake mill (4 wt.%) [76].

$TiMn_2$ is also a promising catalyst material for Mg. Mg-$TiMn_2$ nanocomposite showed outstanding cyclic behaviour, after a 1000 hydrogenation/dehydrogenation cycles sample showed almost no signs of degradation comparing to reference milled pure Mg (Fig. 9). In addition, $TiMn_2$ particles were homogeneously adhered on the surface of MgH_2 even at this stage. Moreover, these particles prevented grain-coarsening process which is highly undesirable for industry applications [77]. The same group also carried a research on $ZrNi_5$ intermetallic compound as a catalyst for Mg [78]. The powder mixture of MgH_2-10 wt.% $ZrNi_5$ was milled for 200 h under hydrogen atmosphere, the product showed impressive kinetics properties being able to absorb and release 5.3 wt.% of H_2 in 1 and 10 min respectively at 275 °C, as an additional achievement, this material can withstand 600 continuous cycles with only a slight capacity loss (from 5.30 wt.% to 4.97 wt.%). As a continuation of this research previously mentioned group introduced Ti_2Ni glassy nano powder into MgH_2 by means of high energy cryo-milling. Resulting product preserved glassy structure (short range order) which is able to withstand temperatures up to 400 °C without crystallisation. This material also demonstrates excellent hydrogenation/dehydrogenation kinetics at relatively low temperatures with appropriate cyclic stability (no significant degradation after 80 cycles) [79]. $LaNi_3$ can also be utilized as catalyst for Mg. It was revealed that after a 100-h milling of MgH_2-7 wt.% $LaNi_3$ powder mixture activation energy was dramatically reduced down to 73.26 kJ mol^{-1} [80]. It was also evident that $LaNi_3$ hard nanoparticles can penetrate MgO layer on the surface of MgH_2 particles creating numerous pores and providing higher conversion degrees - 6 wt.% of hydrogen. In addition, these 6 wt.% can be charged and discharged within 8 or 2 minutes at 200 °C and 225 °C, respectively with excellent cyclic life stability (2000 h) at 225 °C without any signs of degradation.

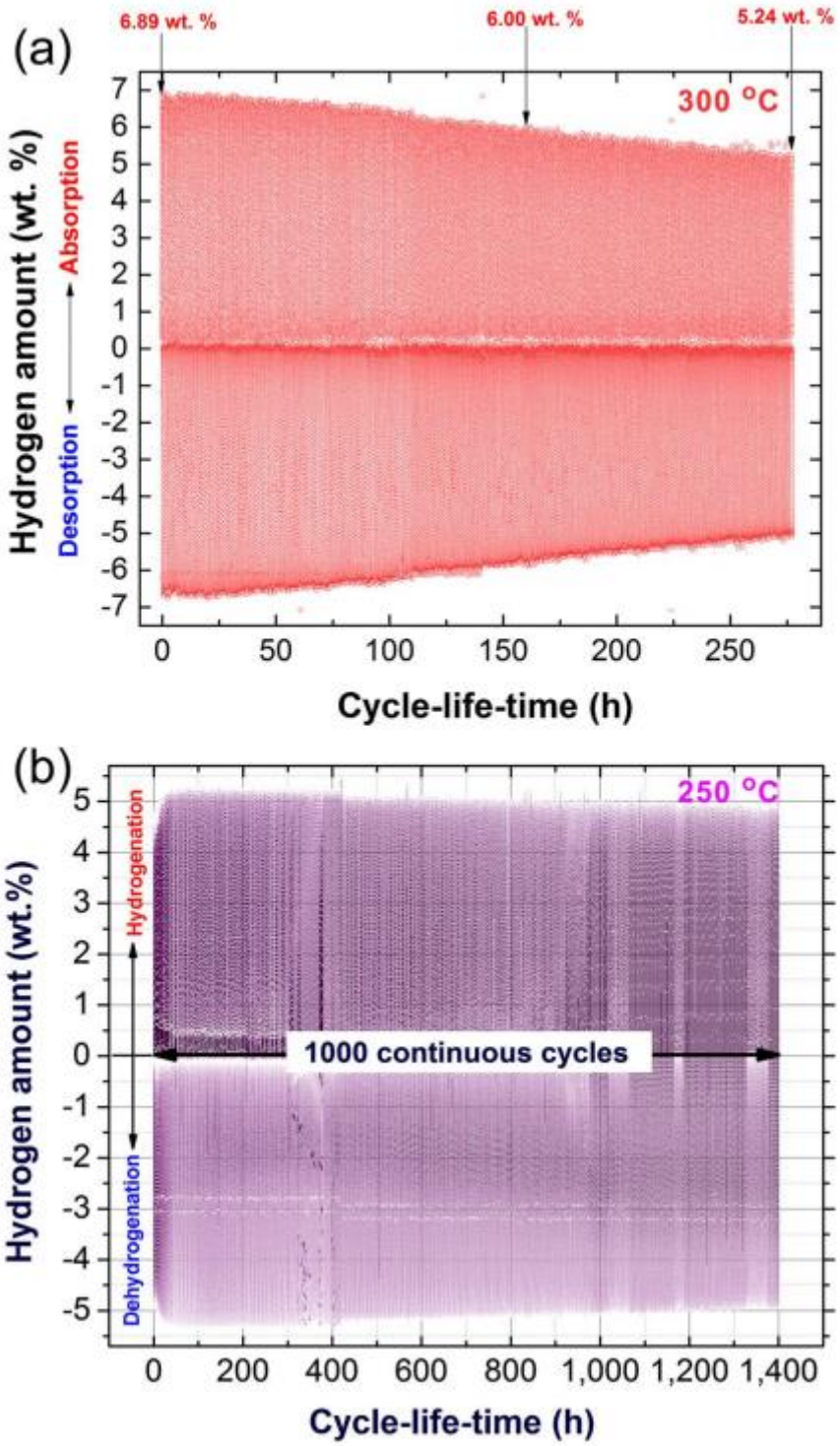

Figure 9. Effect of $TiMn_2$ on cyclability of MgH_2 powders. (a) nanocrystalline MgH_2, (b) nanocrystalline MgH_2/5 wt.% $TiMn_2$ [77]

3.2.2.3 Synergetic catalyst application

Previously listed catalyst additives can cause a significant impact on hydrogen storage properties of Mg on their own. However, recent papers pay special attention on the possibility of

the synergetic catalyst application. Synergetic combinations of different additives can have even greater effect on (de)hydrogenation properties of Mg based hydrogen storage materials [24].

In a recent research it was found that the effect of Ni doped TiO_2 core-shell particles on hydrogen storage properties of Mg [81]. Sample with combined catalyst sowed significantly faster desorption kinetics comparing with only Ni or TiO_2 catalysed samples, especially at lower temperatures (250 °C). It was evident that core-shell particles promote electron transport and hydrogen dissociation consequently, in the same time hard TiO_2 prevents grain growth and stabilize morphology. Co also can be combined with TiO_2 in a form of Co/TiO_2 nanocomposite synthesized through the facile method. Milling of this composite with MgH_2 powder results in a material with relatively low desorption peak temperature (T_{des} = 235.2 °C) compared to only Co catalysed (T_{des} = 329.4 °C) and only TiO_2 catalysed (T_{des} = 288.4 °C) and significantly faster desorption kinetics. Origin of a given synergetic effect comes on the one hand from Co ability to destabilize MgH_2 since the Co-H bond is stronger than Mg-H, on the other hand TiO_2 can donate electron from its conduction band to the metallic Co so that Co/TiO_2 acts as a "nano redox reactor" promoting hydrogen dissociation and recombination [82]. Ni/Ti_3C_2 sandwich particles were synthetized to use them as a catalyst for Mg. It was noted that active electronic interaction between Ni and Ti_3C_2 dramatically improves hydrogen ab/desorption properties of MgH_2. It was also mentioned that Ni promotes hydrogen dissociation and weakens Mg-H bond while Ti_3C_2 can prevent agglomeration of Ni or MgH_2 particles [83].

Often carbon nanostructures are used as a complementary additive to main catalytic materials such as various transition metals and transition metal-based compounds [24]. Graphene oxide-based porous carbon (CG) and titanium chloride ($TiCl_3$) were applied by a given team [84] as catalysts for Mg. As a result of application, desorption kinetics for $MgH_2/CG - TiCl_3$ is in few times faster than for Mg catalysed individually by each of these catalysts. It was suggested that CG acts as a scaffold material, it prevents MgH_2 particles agglomeration and ensures even distribution of $TiCl_3$. In another research N-doped niobium pentoxide ($NbN_{0.9}O_{0.1}$) rods were grown on the surface of the graphene layer. It was evident that these nanorods significantly weaken Mg-H and H-H bonds while graphene can enhance this effect [85]. A couple of papers revealed results on Ni and Co graphene composites used for Mg-based hydrogen storage systems catalysation. Both papers claim significant improvement of dehydrogenisation kinetics and ability of such composite catalyst to preserve catalytic properties [86, 87].

Carbon nanotubes able to generally improve the kinetics including absorption and desorption rates as it will be reviled in this paragraph. In a recent research it was established the effect of TiF_3/MWCNTs catalyst combination on Mg-Ni hydrogen storage nanocrystalline alloy

[88]. Synergetic catalysed sample showed surprisingly fast absorption kinetics which was explained by dissociation acceleration action of TiF_3 and diffusion promotion action of MWCNTs. The effect of synergetic catalysts CNTs with Nb_2O_5 after severe plastic deformation on Mg hydrogen storage properties was investigated by M. Gajdics and Á. Révész [89]. As a result, it was evident that CNTs significantly improve desorption kinetics when added with Nb_2O_5 (Fig. 10). In addition, it was proved by the group that severe plastic deformation even though reduces tube size, it is still preserving their structure. Similar research claims that use of synergetic catalysts in Mg system enables to achieve near theoretical desorption amount values for a given composition (6.43 wt.%) [90].

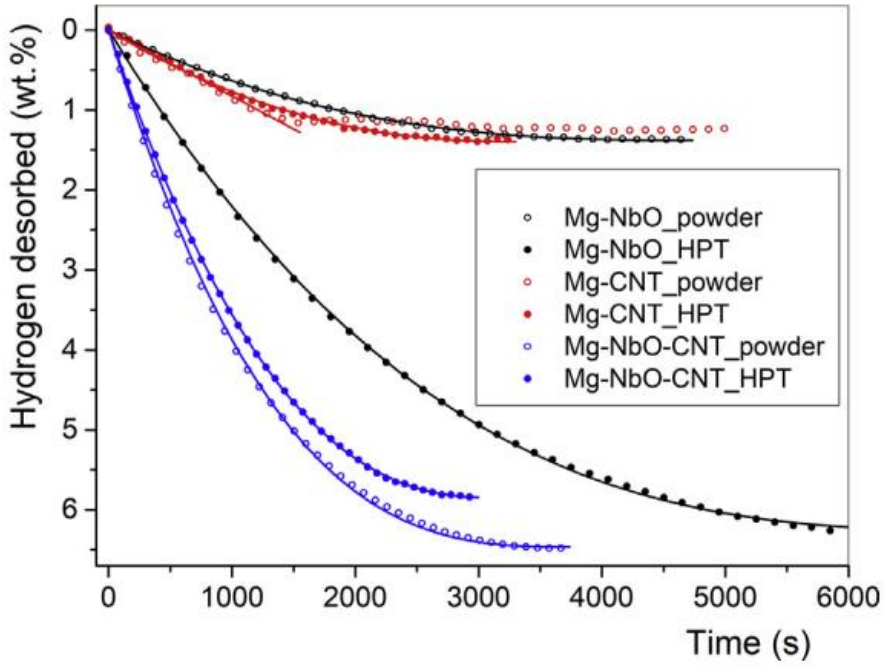

Figure 10. Measured desorption kinetic curves of as-milled powder samples and high-pressure torsion (HPT) discs with synergetic catalysts and without [89]

3.3 Motivation of the research

Hydrogen storage problem solution for hydrogen economy is still unsolved. Besides previously mentioned fundamental problems of classical storage options (gas, liquid) novel hydrogen storage materials both adsorption and absorption based also suffer from various issues. As it was shown, magnesium can be considered as one of the most popular materials for hydrogen storage since its hydride has the largest among all metals hydrogen capacity of 7.6 wt.%, it possess relatively small problems related to hydrogen storage performance (high sorption temperature and poor kinetics) comparing to chemical and complex hydrides and the material itself is relatively

available, cheap and lightweight. Among all catalyst materials FeTi can be emphasized due to several reasons: first, it possesses ability to form hydride, second, majority of papers recognize this catalyst as a composite material [75, 76, 91] omitting the potential of FeTi as small amount catalytic additive and third, FeTi possesses impressive catalytic properties and ability to form Fe_2Ti intermetallic compound. Considering all the above MgH_2 – 10 wt.% FeTi can be a promising object for further investigation.

4 Experimental methods

4.1 Materials and Manufacturing processes

4.1.1 High energy Ball milling

High-energy ball milling is a commonly used method for grain refinement of powders in order to achieve desired nanostructure by application of the severe plastic deformation (SPD) to the initial coarse-grained powder. HEBM is considered as inexpensive, simple, and applicable for wide variety of materials for production of nanocrystalline powders [92].

HEBM can be applied by utilizing various mills among which: vibratory/shake mills, planetary mills and attritors are the most common ones. Vibratory mills (Fig. 11 a) are often used for experimental studies. The powder sample is placed inside of the 0.1-liter vial where 1 g of material with 5-20 g of grinding balls (5:1 – 20:1 ball to powder mass ratio) are subjected to vibration motions in horizontal direction with typical frequency of 20 Hz and motion amplitude of 10-50 mm [93, 94]. The main limitation for such mills is absence of large volumes which limits their application to experimental researches.

Planetary mills usually composed of 2-4 drums (Fig. 11 b) and provide 0.25-1-liter vial capacities. Ball size for such mills and consequently ball to powder ration is higher than for vibration ones. Attritor mills are often used for grinding of ceramic and industry mineral powders. The main distinctive feature of such mills is stationary drum with vertical drive axis, impellers attached to this axis impact balls which consequentially attrit large amounts of powder. However, a characteristic issue of attritor mills is gravity driven powder and balls segregation which keeps a sufficient amount of powder intact near the bottom [92].

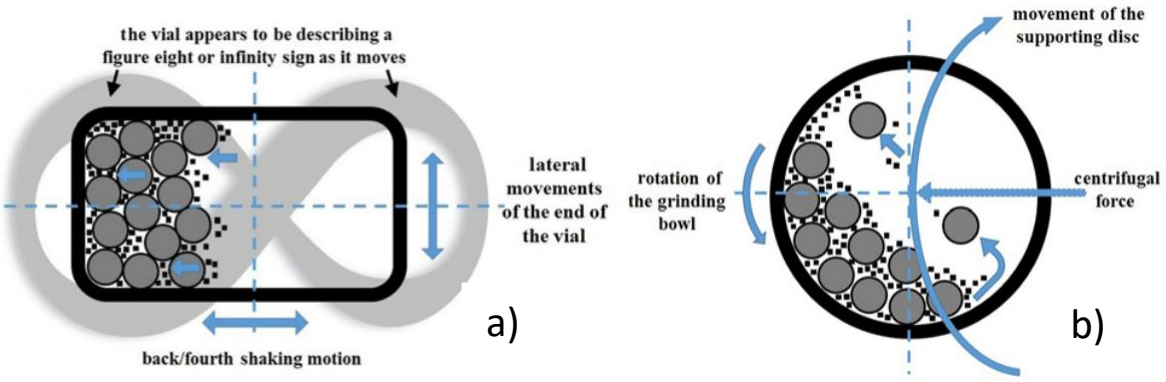

Figure 11. Operation principle scheme for (a) vibratory mill and (b) planetary mill [94]

Figure 12 demonstrates the ball impact on powder agglomerate during milling. During the impact particles can slide, rotate, and rearrange positions due to the particle interaction (Fig. 12). As a result, porosity decrease, until a critical height h' will be achieved where powder particle's mobility is expired (Fig. 12). Further ball motion proceeds with kinetic energy dissipation due to trapped powder particle's elastic and plastic deformation. At the point where all kinetic energy of the ball is dissipated (at the height h'') the ball bounces off exposing powder to another impact [24, 95].

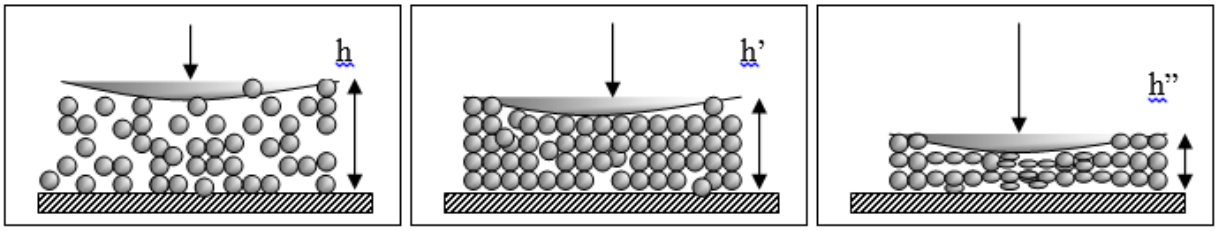

Figure 12. Ball effect on milled powder during the impact [95]

A SPEX-8000 vibratory shaker mill was applied for a current research. Such mills typically constructed of a metallic hull, mobile holder connected to a drive and detachable vial. A holder proceeds figure eight motion with 50 Hz (875 cpm) frequency. Typical vials are made of steel, ceramics or tungsten carbide, their volumes vary from multiple 5 ml sub-sized ones to 75 ml full sized. 65 ml common steel vial can hold from 0.5 g to 10 g of powder which undergoes refinement by hard grinding balls with typical 10:1 ball to powder ratio. Ball impact illustrated previously on Figure 11 enables grain refinement down to nanometres scale for alloys, brittle materials, and composites. Due to such high deformation energy solid state alloying also can occur during longer milling procedures.

In the current research, longest milling procedure was carried during 10 h. For such long-lasting manipulations an essential procedure step is a 15-minute pause after each milling hour to prevent excessive heating which can cause undesirable consequences such as dehydrogenation of utilized MgH_2 and additional oxidation. Another important action which solves problem of uneven powder distribution is vial rotation before each milling initiation. Finally, all powder mixing procedures and vial loading/unloading were proceeded under argon atmosphere in a glow box with only 0.2 % of oxygen content.

4.1.2 Sample preparation

Commercial Fe and Ti powders from Sigma-Aldrich were used as a starting material for catalyst preparation. 2:1 stochiometric amount of these powders was mixed under argon

atmosphere in a "home-made" glow box. Two portions from this mixture were milled in the SPEX 8000 mill with 10:1 ball to powder mass ratio during 3h (FeTi(3h)) and 10h (FeTi(10h)). Thereafter the FeTi(10h) catalyst was mixed with MgH_2 powder in a 1:9 mass ratio (10 wt.% of catalyst) to obtain 1 g of MgH_2/FeTi powder mix. This procedure was conducted for 3 different milling times for 1h, 3h and 10h separately obtaining MgH_2/FeTi(1h), MgH_2/FeTi(3h) and MgH_2/FeTi(10) powders respectively. General information regarding different samples is listed in the Table 1.

Table 1. Ball milling parameters

Sample	Material Ratio	Milled Amount	Ball-to-Powder Ratio	Milling Time
MgH_2/Fe_2Ti(1h)	9:1	1g	10:1	1h
MgH_2/Fe_2Ti(3h)				3h
MgH_2/Fe_2Ti(10h)				10h

4.2 Characterization methods

4.2.1 Hydrogen sorption instrument

A Sieverts'-type apparatus (Fig. 13) was used for absorption/desorption measurements. Its main structural elements can be described as: hydrogen supplier (high pressure tank) connected through the valve with the sample chamber which also has valve connection with the pump. Manometer is attached to the specimen chamber in order to conduct pressure measurements. To conduct absorption measurements the sample chamber should be loaded with some dehydrogenated powder sample and filled with hydrogen up to a certain pressure value, consequent pressure decrease provides absorption kinetics. For desorption measurements pump should decrease pressure down to a certain value inside of the sample camber filled with hydrogenated powder specimen, consequent pressure increase provides desorption kinetics. Precise pressure measurements are processed according to known calibrated volumes. Typically, such measurements require some heating to achieve desired sorption temperature, detailed discussion regarding sorption kinetics and thermodynamics is presented in corresponding paragraphs.

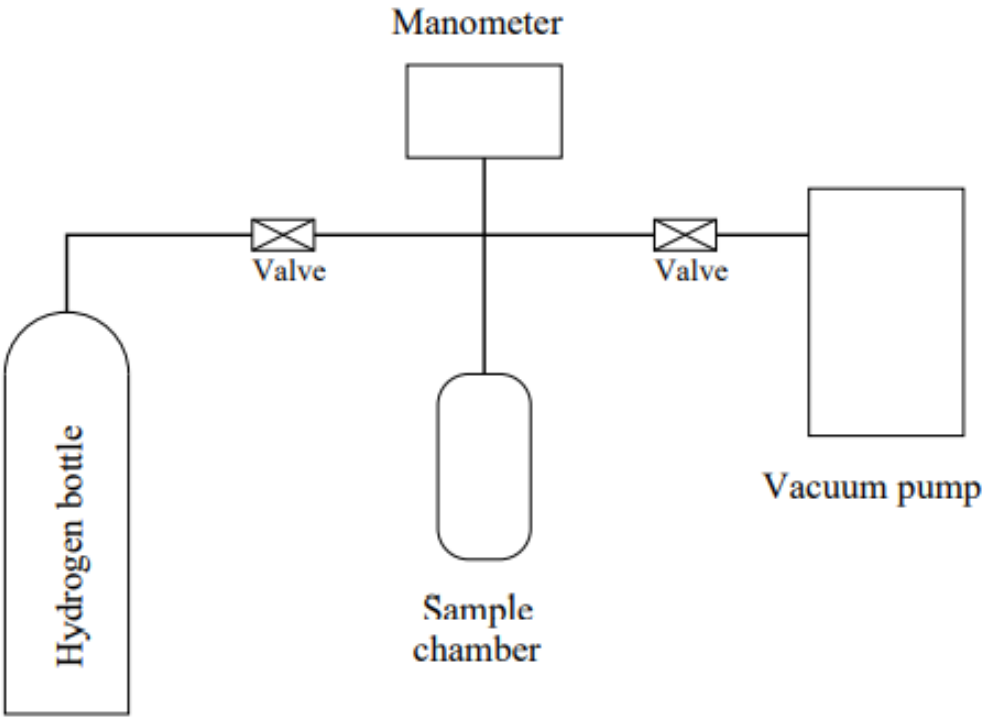

Figure 13. Sieverts'-type instrument scheme [30]

For the current experiment several absorption/desorption cycles were proceeded at 573 K. Initial pressure values were set at p_{abs} = 1 MPa, p_{des} = 1 kPa. The measurements were conducted in a "home-made" Sieverts'-type instrument in Sofia University. Absorption/desorption measurements were stopped when corresponding processes reached saturation.

4.2.2 Scanning Electron Microscopy

Scanning electron microscope (SEM) is a type of electron microscope that focuses accelerated electrons in a small sample area and detects various products of electron-sample interaction. Typical products are back scattered electrons (BSE), secondary electrons (SE) and characteristic X-ray radiation. The technique provides detailed information about sample morphology and elemental composition. BSE data can be especially useful for samples with two phases which composed of different elements with significant gap in mass numbers since BSE intensity is higher for heavier nuclei.

In a current research a tabletop TM4000Plus SEM instrument was used. BSE, SE and Mix (BSE+SE) regimes were used to investigate sample surface. Energy-dispersed X-ray spectroscopy (EDS) analysis was also applied to determine chemical composition of powders. Measurements were carried at 15 kV of accelerating voltage.

4.2.3 Transmission Electron Microscopy

Transmission Electron Microscope (TEM) is a type of electron microscope that transmits accelerated electrons through a thin (less than 100 nm) specimen consequentially forming image. TEM can also be used to obtain phase composition via detection of diffracted electrons.

In this work high resolution TEM (HRTEM) JEOL JEM-3010 (KFKI institution) 300 kV microscope was used to investigate the microstructure of the MgH_2/FeTi(3h) powder. The TEM sample was prepared by mixing the powder with G-2 epoxy resin, thereafter thin layer of this mixture was placed between two Si plates and heated 3 times up to 100°C, 110°C and 120°C. Argon beam etching was applied to create a small hole in this structure. As a result, several small particles close to the edge of the hole were transparent to the electron beam. Obtained images were processed by GATAN Digital Micrograph software.

4.2.4 X-ray diffraction (XRD)

XRD is a non-destructive technique which can be used to investigate microstructure of crystalline materials. It is based on the successful interference of monochromatic X-rays scattered from a regular array of some scattering centres (crystalline planes). Usually scattered waves cancel each other, but at a specific angles (2θ) between the incident and the scattered beam these waves can sum up resulting in a great intensity peak. These specific scattering angles are related to various lattice spacings (d_{hkl}). This means that if a certain condition (Bragg's conditions) is satisfied there will be an intensity peak, which can be determined by:

$$2d_{hkl} \sin\theta = \lambda, \tag{12}$$

where λ – wavelength of the incident X-ray beam. Bragg's law schematic representation is presented on the Figure 14.

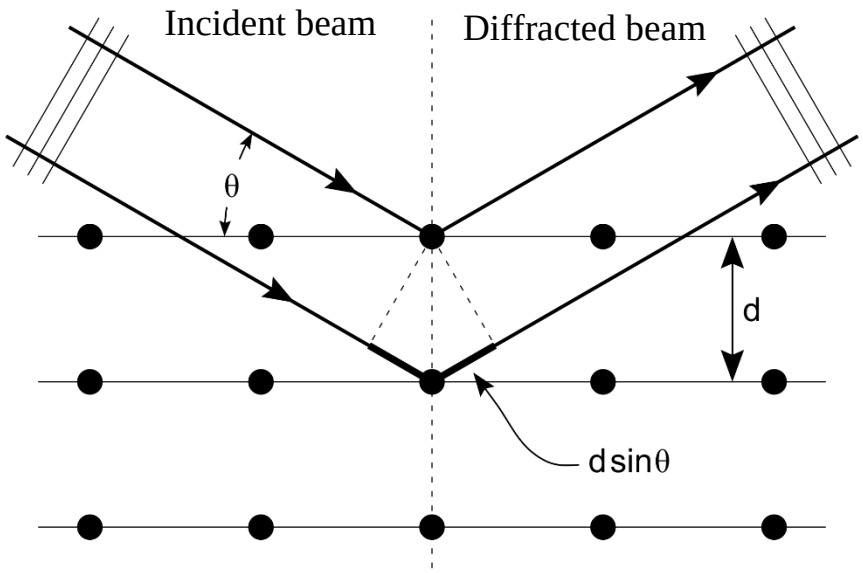

Figure 14. Schematic representation of the Bragg's law

A Smartlab diffractometer (Rigaku, Japan) was used in yhe current research to conduct XRD measurements of powder samples. CuKα x-rays (λ = 0.15418 nm) with Bragg-Brentano geometry were applied to obtain diffraction patterns.

4.2.5 Calorimetry

Power compensated differential scanning calorimeter (DSC) was used to investigate dehydrogenation process of the hydrided powders (Fig. 15). Differential calorimeters contain 2 sections, one with reference sample and one with investigated sample. Both sections are linearly heated in time with a constant heating rate. Specifically, for power compensated calorimeter, the temperature difference between the sample and the reference is compensated by changing power applied to the heating elements. Such instruments can be used to detect all kinds of endo- and exothermic processes. The basic function that describes the detected heat flow (w) signal between the reference and the sample can be given as

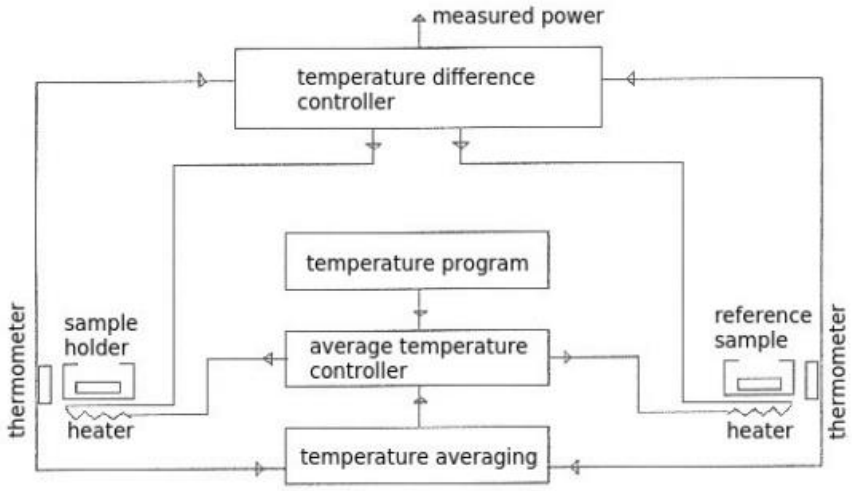

Figure 15. Feedback system of DSC

$$w = \frac{dh}{dt} + (C_m - C_r)u + w_{bas}(T) \quad , \tag{13}$$

where $\frac{dh}{dt}$ – the rate of the exothermic or endothermic transformation, C_m and C_r – heat capacity of the sample and the reference respectively, u – heating rate, $w_{bas}(T)$ – term which describes the baseline. In a current research all hydride containing samples were subjected to 2 heating cycles with 40 K/min heating rates in the 320 – 950 K heating range under protective Ar atmosphere. Samples were placed in aluminium crucibles.

5 Results and discussions

5.1 Characterisation of pre-milled catalyst

As it was mentioned in [75, 76], pre-milling of catalyst is a beneficial step which can improve catalytic properties of Fe-Ti by achieving desired phase composition (such as FeTi solid solution and Fe_2Ti intermetallic compound). SEM measurements were applied to investigate microstructure of the pre-milled FeTi(10h) sample. It can be seen in Figure 16 that obtained powder has significant particle and aggregate size inhomogeneity. Powder particles have clearly visible sharp edges appeared due to SPD induced by HEBM. Aggregates visibly possess flat surfaces due to powder – vial contact. Particle size varies roughly from 2 μm up to 20 μm while some large particle aggregates can reach up to 150 μm.

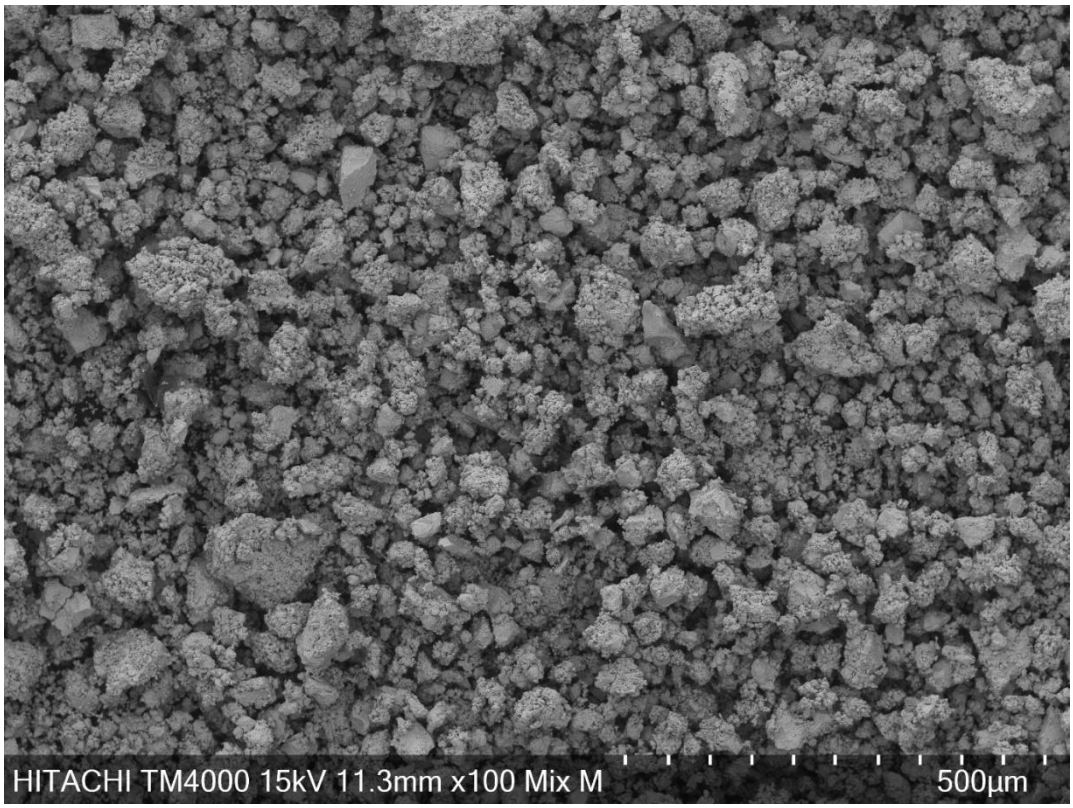

Figure 16. Low magnification (BSE) SEM image of FeTi(10h) pre-milled catalyst powder

Figure 17 represents The XRD patterns of the unmilled Fe-Ti powder mixture (FeTi(mix)), FeTi(3h) and FeTi(10h) samples. It clearly shows that all Ti is consumed during milling due to solid state alloying reaction, and as a result, formation of Fe-Ti solid solution ($Fe_{0.975}Ti_{0.025}$) takes place. According to XRD patterns, FeTi(3h) sample contains only the $Fe_{0.975}Ti_{0.025}$ solid solution phase while FeTi(10h) sample clearly contains hints of Fe_2Ti intermetallic phase among $Fe_{0.975}Ti_{0.025}$ related peaks. Therefore, it is evident that longer milling time may lead to formation of Fe_2Ti intermetallic phase in sufficient quantities. Yet still, Fe-Ti solid solution phase can be

considered as predominant after 10h of milling. As a result of this experiments series, FeTi(10h) was chosen as a catalyst material for addition to the commercial MgH_2 by HEBM.

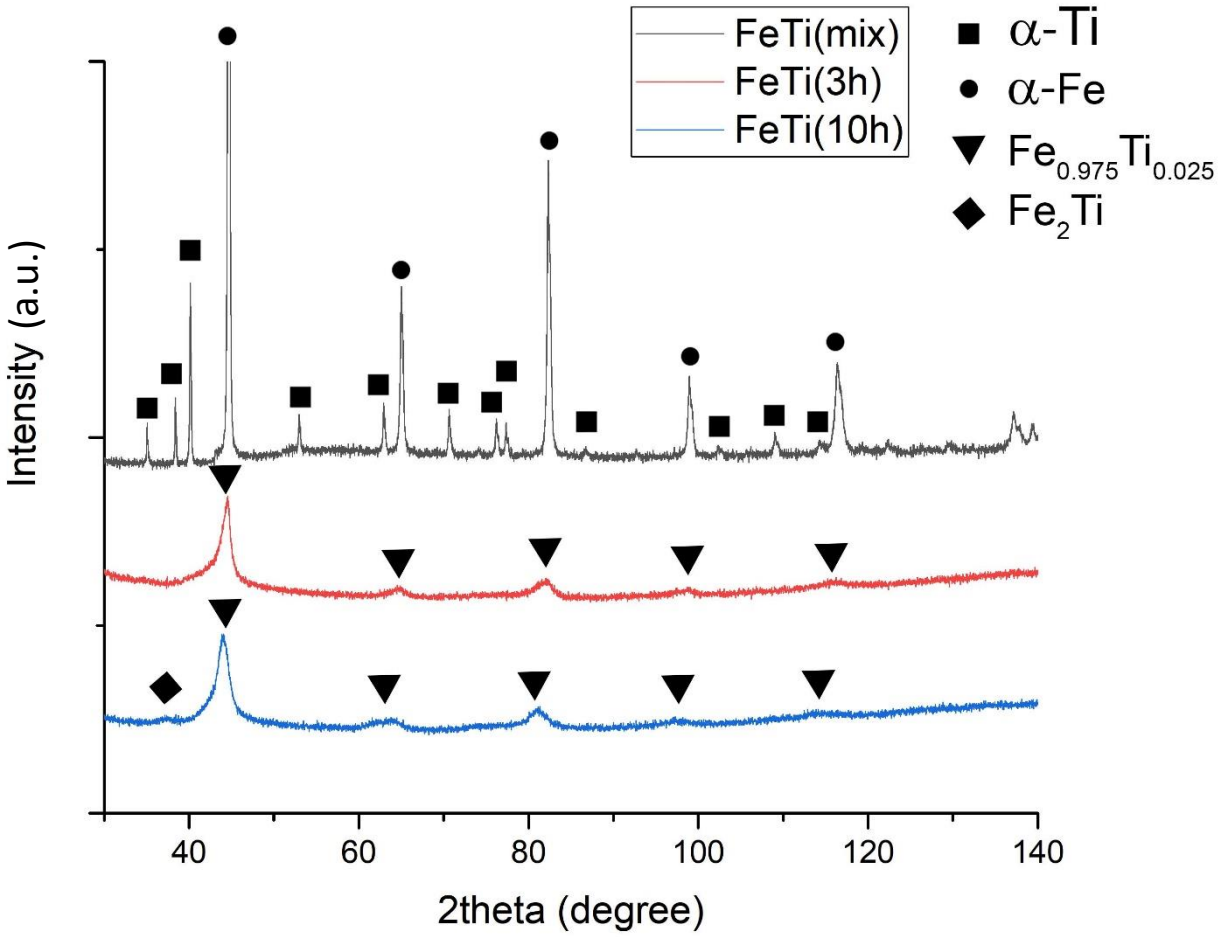

Figure 17. XRD patterns of FeTi(mix), FeTi(3h) and FeTi(10h) catalyst powders

5.2 Characterisation of MgH_2/FeTi samples

5.2.1 Scanning Electron Microscopy

As a common feature of the MgH_2/FeTi milled powders, all of them contain large flat surface agglomerates (Fig. 18 a, b, c) of the corresponding micrographs. Such agglomerates may appear due to powder – vial wall interaction, when soft powder sticks to hard flat surfaces. Nevertheless, the MgH_2/FeTi(10h) powder seems significantly more refined with absence of large flattened agglomerates.

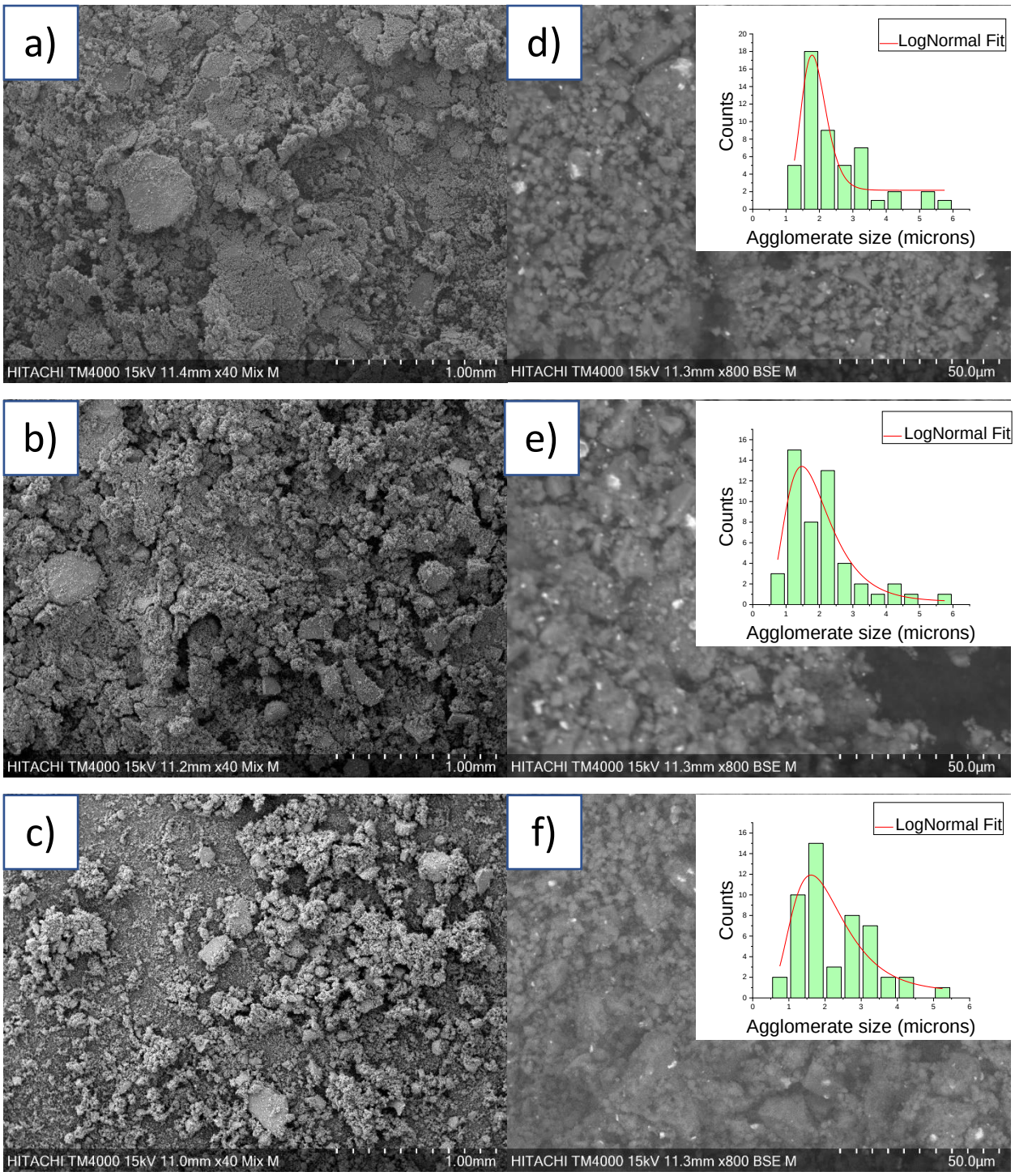

Figure 18. Low magnification (BSE+SE) and high magnification (BSE) SEM images with corresponding particle log-normal size distributions for a, e) MgH_2/FeTi(1h), b, f) MgH_2/FeTi(3h) and c, g) 1 MgH_2/FeTi(10h) samples.

Brighter spots on the enlarged BSE images correspond to FeTi particles (Fig. 18 d, e, f). As it can be seen, catalyst agglomerates are qualitatively smaller than the hydride ones. Also, catalyst particles are not isolated, instead they pressed into the surface of hydride agglomerates. In

addition, even catalyst distribution for all samples can be concluded as a result of qualitative observation. Particle sizes for the hydride samples were determined by ImagePro+ using linear intercept method based on 50 counts. It was found that the histograms adequately follow a log-normal size distribution (see the insets), which is typical for SPD attrited powder particles. Resulting particle size for MgH_2/FeTi(1h) sample was obtained as 1.85±0.08 μm, for MgH_2/FeTi(3h) sit was 1.79±0.21 μm and for MgH_2/FeTi(10h) was 1.96±0.37 μm. It appeared to be evident that all samples have similar particle size, below 2 μm with minor differences.

EDS measurements represent chemical composition of the hydrided samples. According to Table 2 all samples are dominated by Mg with an average at 92 – 94 wt.%, however hydrogen cannot be detected by EDS since it has only 1 electron. As one can also recognise, some portion of catalyst is missing, only 6.02 wt.% for MgH_2/FeTi(1h) sample, 8.20 wt.% for MgH_2/FeTi(3h) and 8.54 wt.% for MgH_2/FeTi(10h) while nominal amount is 10 wt.% for each. There are couple reasons of such discrepancy: first, since FeTi particles are much more dense than host material, therefore they may stick near edges and at walls of milling vial, second, Fe/Ti mixture was pre-milled for 10h which results in a longer exposure time and as a consequence higher oxidation degree. The lower catalyst content for the MgH_2/FeTi(1h) catalyst comparing to MgH_2/FeTi(3h) and MgH_2/FeTi(10h), may be explained by the lack of catalyst distribution homogeneity due to comparably smaller milling period and absence of vial rotation procedures which were performed for other samples after each hour. It should also be noted that large amounts of oxygen can be found in all SEM samples, therefore a correction was applied to exclude this undesired element. The reason of such significant oxygen amount is long exposure time to air.

Table 2. EDS data for the MgH_2/FeTi powders

	MgH_2/FeTi(1h)			MgH_2/FeTi(3h)			MgH_2/FeTi(10h)		
Element	Weight (wt.%)	Corrected weight (wt.%)		Weight (wt.%)	Corrected weight (wt.%)		Weight (wt.%)	Corrected weight (wt.%)	
Fe	2.59	4.26	6.02	3.54	5.82	8.20	3.82	6.25	8.54
Ti	1.07	1.76		1.45	2.38		1.40	2.29	
Mg	57.14	93.98		55.84	91.80		55.89	91.46	
O and other	39.09	-		38.84	-		38.85	-	

5.2.2 X-Ray diffraction

XRD patterns of the MgH_2/FeTi powders can be seen on the Figure 19. Since diffractogram provide phase composition, all samples contain three phases. According to corresponding database all samples contain α tetragonal and γ high pressure orthorhombic MgH_2 phases which evidently appear during milling procedure. It is also evident from the patterns that α phase fraction is significantly higher than γ for all samples. A third phase is MgO confirmed by a broad diffraction peak in the middle of patterns ($2\theta \approx 45°$) which quantitatively low for all three samples. No clearly visible signs of catalyst material can be seen on the patterns, which relates to the volumetric issue, i.e. the presence of catalyst is hindered on the patterns most probably due to the small volume fraction.

With increasing milling time Bragg-peaks are significantly reduced in height and increased in width which can be explained by intensive grain refinement and overall defect generation during milling. As one can also notice there are some low intensity Bragg-peaks corresponding to the MgH_2/FeTi(1h) powder, which cannot be identified.

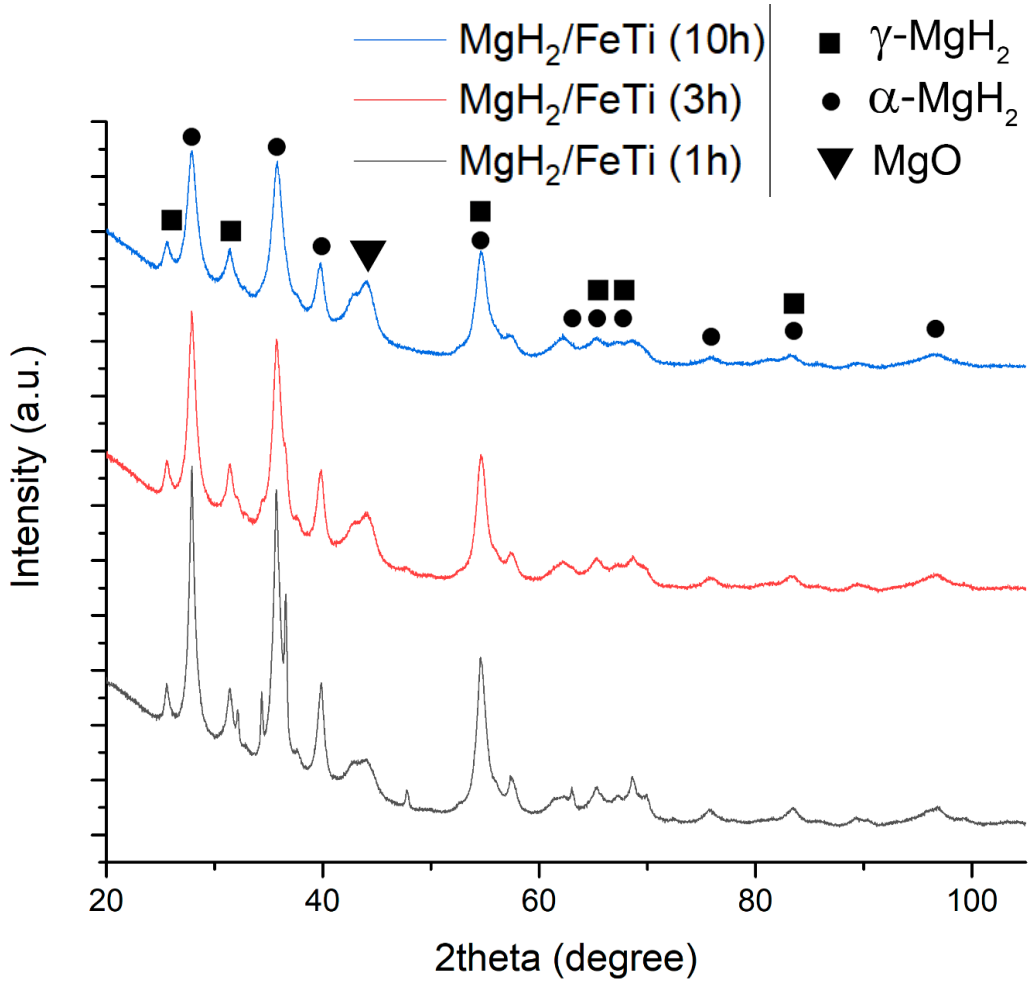

Figure 19. XRD patterns of the MgH_2/FeTi samples

Williamson-Hall (WH) method was applied to determine crystallite size of the milled powders [96]. In this analysis full width at half maximum of the Bragg-peaks (ΔK) corresponding to a distinct phase is plotted against the magnitude of the diffraction vector (K), where:

$$\Delta K = \frac{2\cos\theta(\Delta\theta)}{\lambda}, \tag{14}$$

where θ and Δθ are position and the width of a diffraction peak, respectively and

$$K = \frac{2\sin\theta}{\lambda}. \tag{15}$$

The total peak broadening can be represented as:

$$\Delta K = \Delta K^{SIZE} + \Delta K^{STRAIN} = \frac{0.9}{D_{WH}} + A\langle\varepsilon^2\rangle^{\frac{1}{2}}K\ , \tag{16}$$

where ΔK^{SIZE} is a size broadening, ΔK^{STRAIN} on the other hand, is a strain broadening, D_{WH} – crystallite size, A – constant of unity. WH plots for MgH_2/FeTi(3h) and MgH_2/FeTi(10h) samples are featured in the Figure 20. Four proper peaks for α-MgH_2 with 2θ angles and corresponding Miller indices (27.9° (110), 35.8° (101), 54.7° (211) and 65.4° (310)) were taken to plot the values. Intersects were obtained as ΔK = 0.100±0.021 nm^{-1} for MgH_2/FeTi(3h) and ΔK = 0.100±0.013 nm^{-1} for MgH_2/FeTi(10h), corresponding crystallite sizes are D_{WH} = 9.97±0.22 nm and D_{WH} = 10.01±013 nm, respectively.

Calculated mean atomic displacement values are $\langle\varepsilon\rangle \approx 0.003$ for MgH_2/FeTi(3h) and $\langle\varepsilon\rangle \approx 0.008$ for MgH_2/FeTi(10h), which clearly indicates that longer milling time results in a larger atomic displacement. It is noted that a significant discrepancy from linear behaviour on the WH plots is caused by the strain anisotropy generated by dislocations.

In conclusion, crystallite size determined from X-ray line profile broadening appeared to be in nanometres range (~10nm), while particle size obtained from SEM images is in couple of microns range. It is evident that crystallite size probably reached its saturation even before 3 hours of milling.

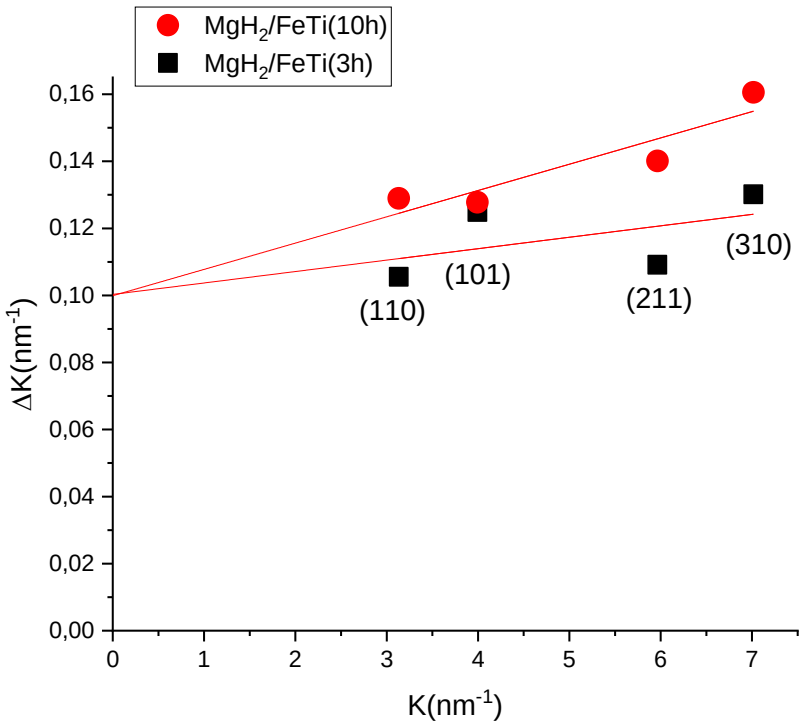

Figure 20. WH plots for MgH_2/FeTi(3h) and MgH_2/FeTi(10h) tetragonal samples

5.2.3 Transmission Electron Microscopy

Figure 21 presents a typical region of the MgH_2/FeTi(3h) powder. As one can realize, the selected area is abundant in nanocrystals (denoted by dashed circles) with D_{TEM} ~ 10 nm. This value undoubtedly correlates with the XRD crystallite size (D_{WH}). These crystallites can be distinguished by parallel atomic planes. It is noted that these nanocrystals relate to Mg (hexagonal) phase, which was detected everywhere by electron diffraction measurements, probably due to the high energy interaction between incident argon atoms with hydrogen. This effect might be the reason why TEM studies on MgH_2 are rarely found in the literature.

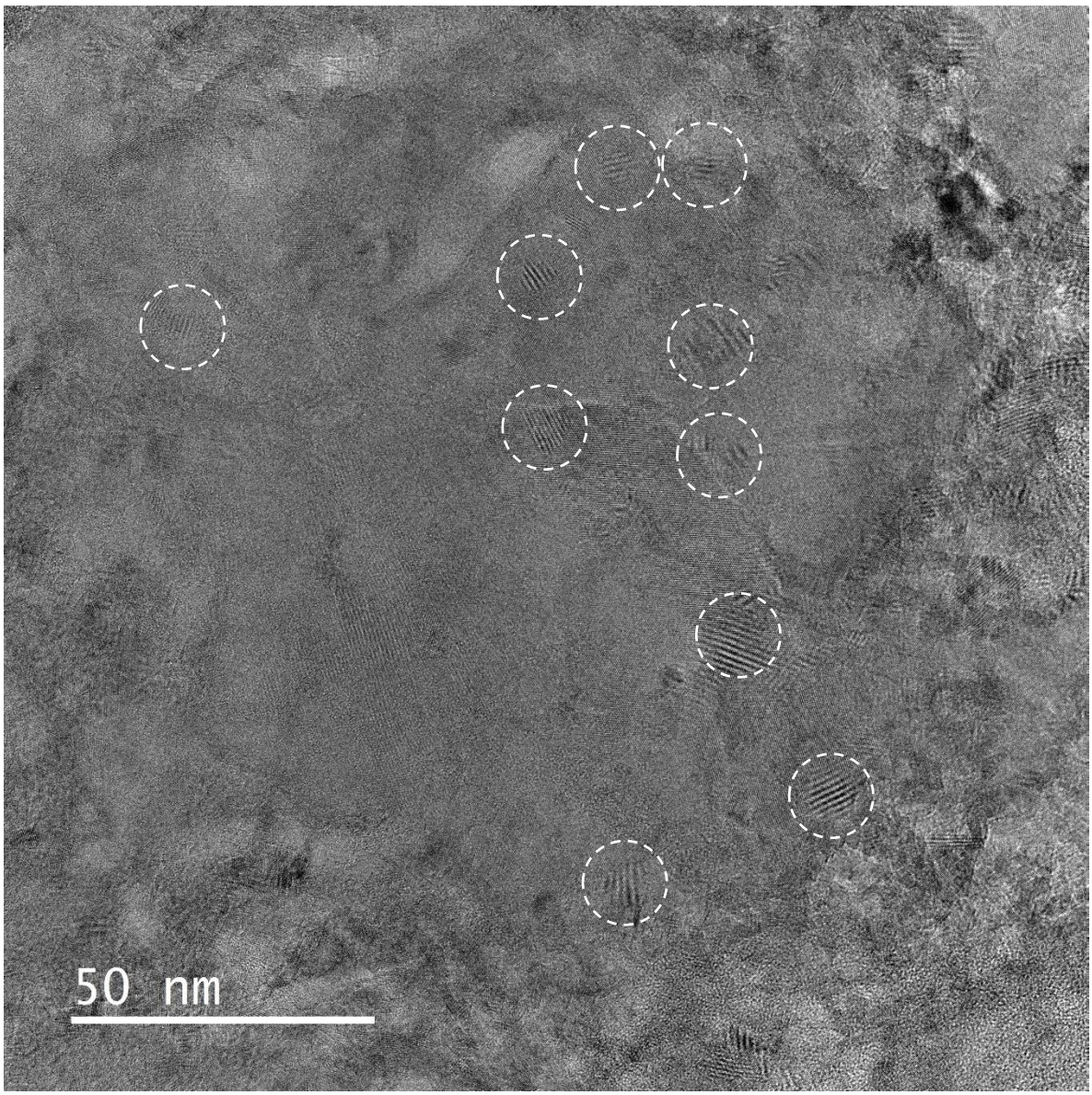

Figure 21. High magnification TEM image of MgH_2/FeTi(3h) powder particle

5.2.4 Calorimetry

For all the MgH_2/FeTi powders Linear heating calorimetry was performed at temperatures between 320 – 950 K as it fixed in the Chapter 4.2.4. Figure 22 represents the of 1st heating runs for all hydride samples. It clearly shows presence of two endothermic peaks which related to dehydrogenation of the α and γ phases. It is assumed that the first peak (T1) can be related to the α phase due to a lower thermal stability of Mg-H bond, while second peak (T2) relates to the γ phase.

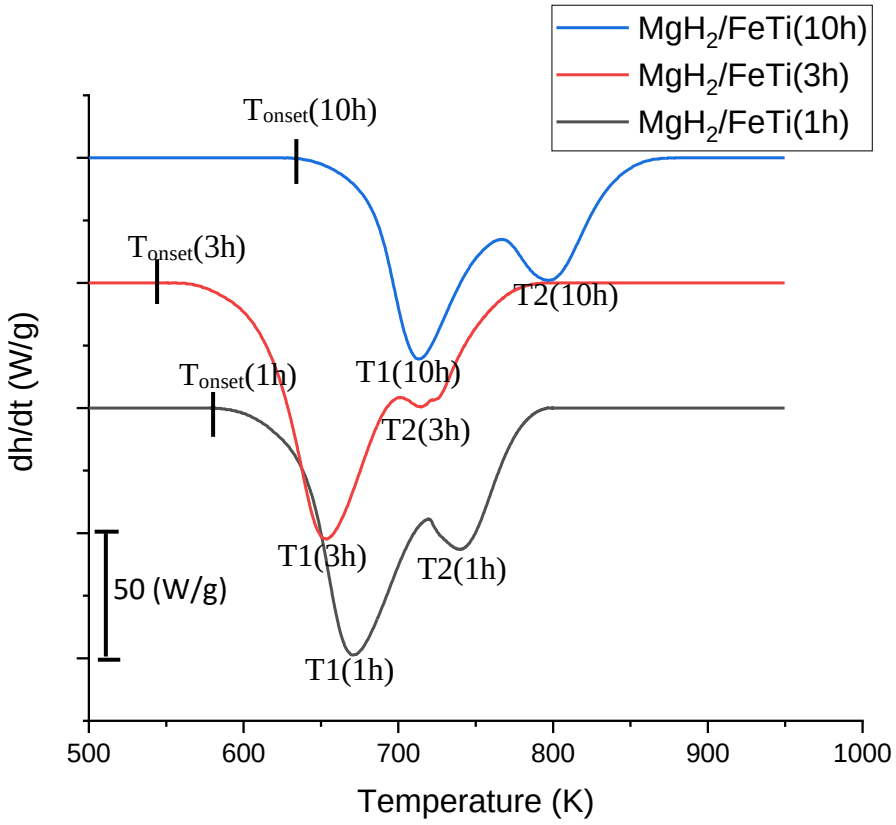

Figure 22. 1st calorimetry heating cycle for MgH_2/FeTi powders

According to quantitative information listed in the Table 5, MgH_2/FeTi(3h) sample shows the onset of dehydrogenation (T_{onset}) at the lowest temperature. Desorption peaks for MgH_2/FeTi(3h) sample also shifted towards lower temperatures which directly proves its best desorption performance. In addition, total enthalpy uptake (ΔH) values are similar for all samples, therefore the

$$\alpha - MgH_2 \rightarrow Mg + H_2, \quad (17)$$

$$\gamma - MgH_2 \rightarrow Mg + H_2 \quad (18)$$

dehydrogenation reactions are completed. Minor differences between ΔH values may be caused by different α/γ ratio.

Table 5. Characteristic thermal parameters of the MgH_2/FeTi powders

Sample	Desorption start (K) (T_{onset})	1st Peak (K) (T1)	2nd Peak (K) (T2)	Desorption end (K) (T_{end})	ΔH (J/g)
1h-milled	579	670	739	796	-12616
3h-milled	549	653	713	793	-12906
10h-milled	629	712	796	880	-11151

T1 and T2 positions with respect to the milling time clearly define the presence of an optimal milling time for MgH_2/FeTi samples. As it can be seen in Figure 23, the MgH_2/FeTi(3h) sample possesses the lowest stability against dehydrogenation among all samples. Moreover, longer milling time (10h) negatively affects desorption peak position, shifting it towards even higher temperatures comparing to short milling time (1h).

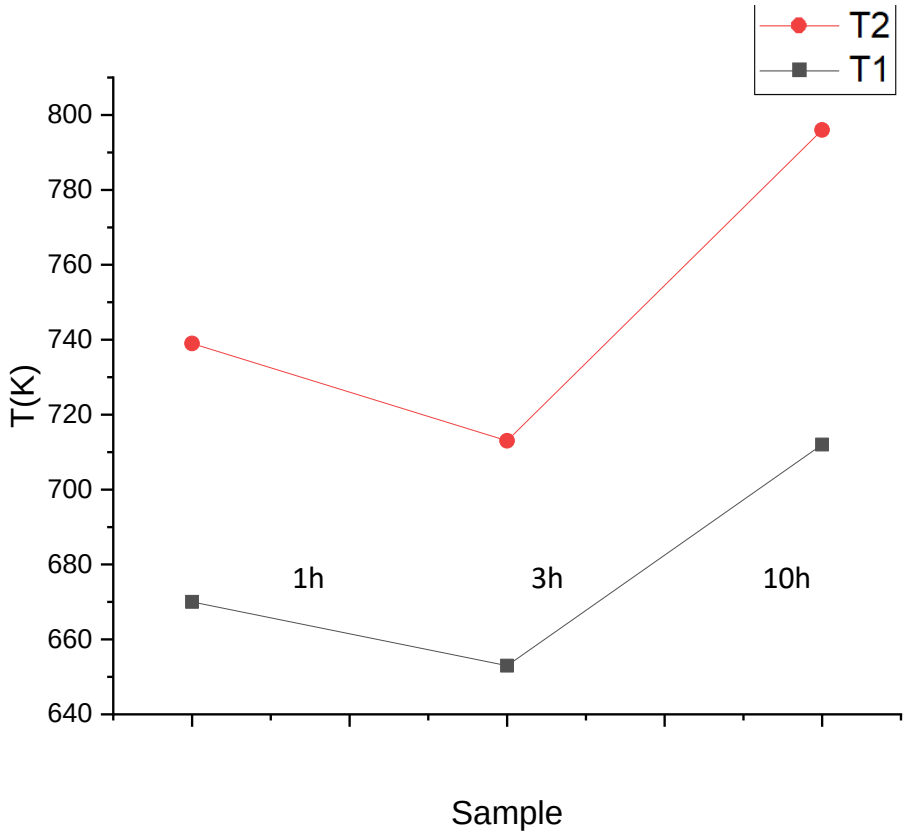

Figure 23. Peaks positions with respect to the milling time

Figure 24 presents the first and the second heating runs of the MgH_2/FeTi(3h) sample. In can be clearly seen that α phase possesses higher stability since it appears during the 2nd cycle, while there is no hint of the less stable γ phase.

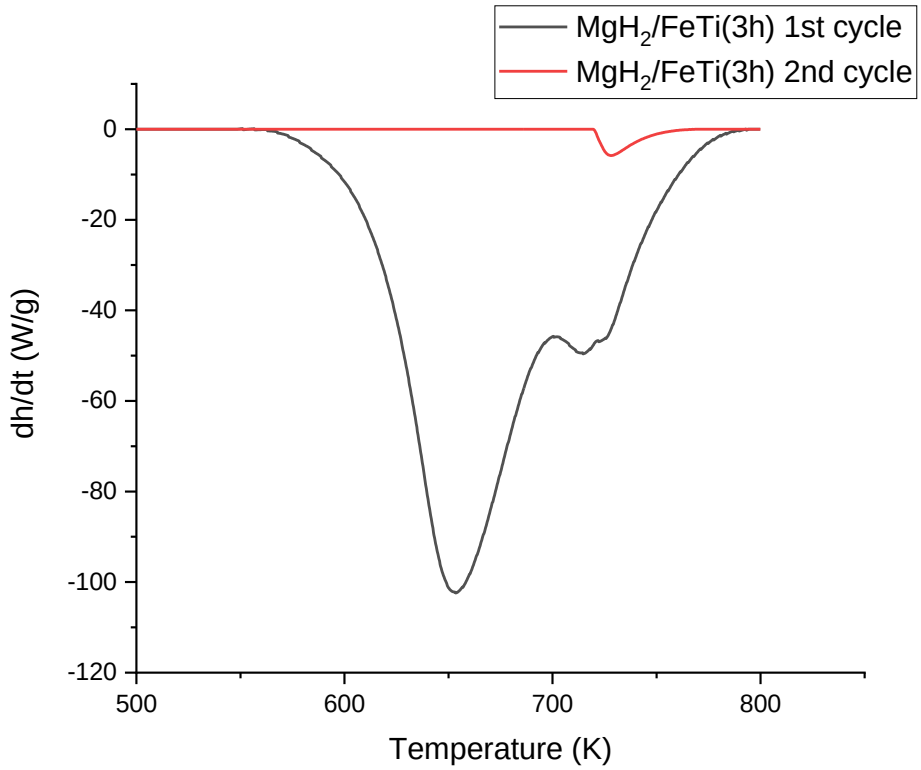

Figure 24. 1st and 2nd calorimetry cycles for MgH_2/FeTi(3h) sample

Figure 25 represents the XRD pattern for MgH_2/FeTi(1h) sample taken after two dehydrogenation cycles. It clearly shows that Mg is dominant, no hint of any MgH_2 phase is present which indicates perfect dehydrogenation of the sample. On the other hand, very sharp diffraction peaks can be seen on the pattern, corresponding to defect elimination and significant crystallite growth due to a heating process. MgO Bragg-peak intensity is almost the same as for as-milled MgH_2/FeTi(1h) sample which indicates absence of additional oxidation during the experiment.

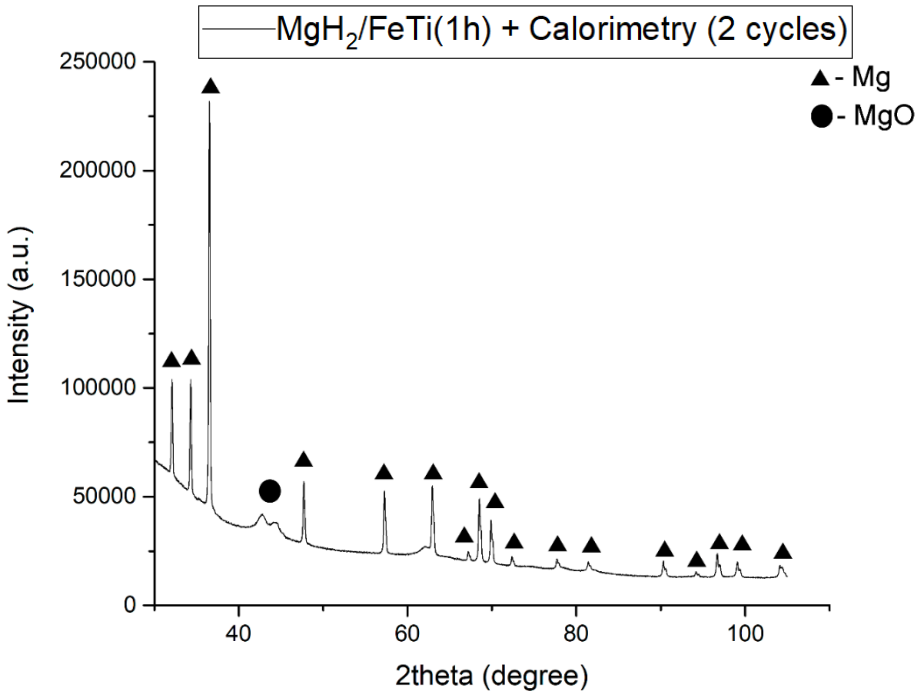

Figure 25. XRD pattern for the MgH_2/FeTi(1h) after 2 calorimetry cycles

5.2.5 Sorption

The results of absorption/desorption experiment performed on the MgH_2/FeTi samples after several activation cycles can be seen on Figure 26. As one can notice, all MgH_2/FeTi powder samples can uptake a significant amount of hydrogen in a reasonably short time. The first thing which can be pointed is outstanding sorption performance of MgH_2/FeTi(3h) powders. According to the Table 6, MgH_2/FeTi(3h) was able to absorb 6.9 wt.% of hydrogen in total which is close to the theoretical value 7.00 wt%, also it was able to absorb 5.2 wt.% in 10 minutes, showing excellent kinetics. On the other hand, MgH_2/FeTi(1h) and MgH_2/FeTi(10h) samples absorbed only 2.5 wt.% and 1.2 wt.% in 10 minutes, respectively. Therefore, the initial sorption kinetics for MgH_2/FeTi(10h) is the slowest, although it was capable to totally absorb more than MgH_2/FeTi(1h), as seen in Table 6.

As seen in Figure 26, Desorption is almost complete for all powders, in accordance with the XRD study (Fig. 25). Despite the fact that MgH_2/FeTi(3h) sample definitely possesses exceptional absorption kinetics, it has only a minor lag in desorption kinetics with respect to MgH_2/FeTi(1h) which was able to desorb 2.3 wt.% in 10 minutes comparing to 2.8 wt.% for MgH_2/FeTi(3h). Moreover, total desorption value for MgH_2/FeTi(1h) (6.1 wt.%) is slightly higher

than for MgH_2/FeTi(3h) (5.7 wt.%). As in the case of absorption, MgH_2/FeTi(10h) possesses the poorest desorption kinetics being able to desorb only (0.8 wt.%) in 10 minutes.

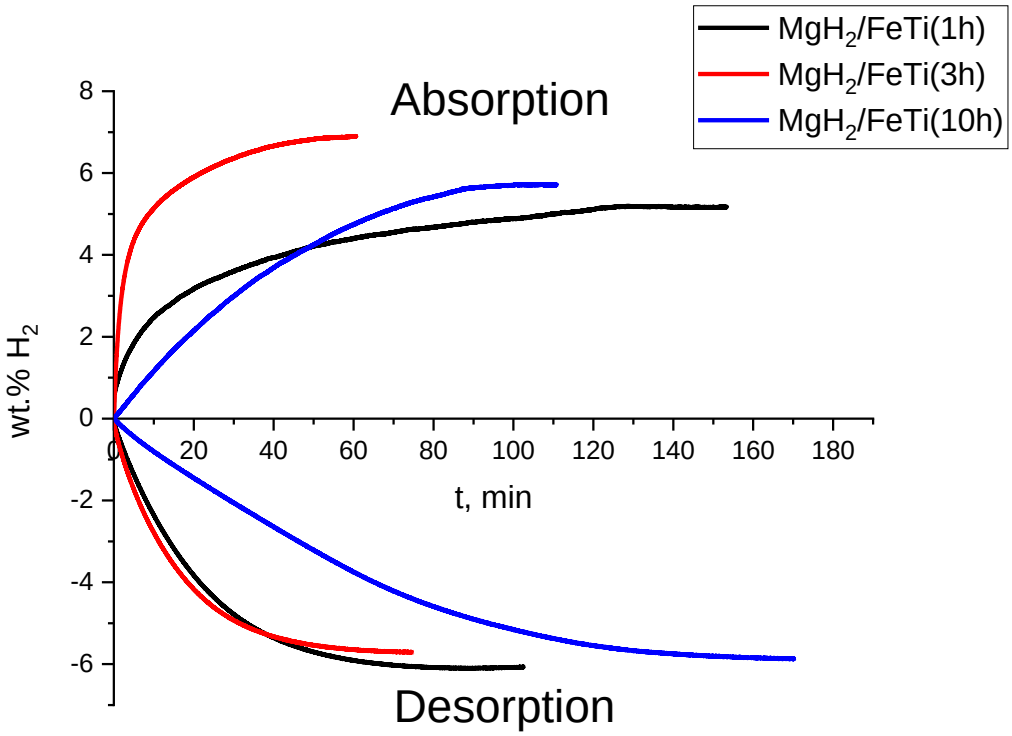

Figure 26. 2nd sorption/desorption curves for MgH_2/FeTi samples

Table 6. Sorption experiment results

Sample	Total absorbed hydrogen (wt.%)	Absorbed hydrogen at 10 min (wt.%)	Total desorbed hydrogen (wt.%)	Desorbed hydrogen at 10 min (wt.%)
MgH_2/FeTi(1h)	5.2	2.5	6.1	2.3
MgH_2/FeTi(3h)	6.9	5.2	5.7	2.8
MgH_2/FeTi(10)	5.7	1.2	5.9	0.8

As one can notice, the JMA function can satisfactorily fit all normalized absorption (Fig. 27 a, b, c) and desorption (Fig. 27 d, e, f) measurements, see equation (3 a). For better visualisation equation (3 a) can be transformed into:

$$\ln(-\ln(1-\alpha)) = \mathrm{n}\cdot\ln(t) + \ln(k) \qquad (19)$$

Accordingly, the $\ln(-\ln(1-\alpha))$ vs. $\ln(t)$ plot should be a straight line, whose slope provides n, while the intercept gives $\ln(k)$. Such transformed functions can be seen in Figure 28

for all, absorption and desorption measurements. In general, the absorption functions well follow the linear behaviour (Fig. 28 a), therefore it is concluded that these processes can be described by a single JMA exponent throughout the entire hydrogenation. These values are listed in Table 7. For the transformed desorption functions the fits are not so perfect (Fig. 28 b), especially for the MgH_2/FeTi(10h) powder a significant deviation from the linear relationship takes place at early stage of desorption. This phenomenon corresponds to a slight change in n-JMA parameter.

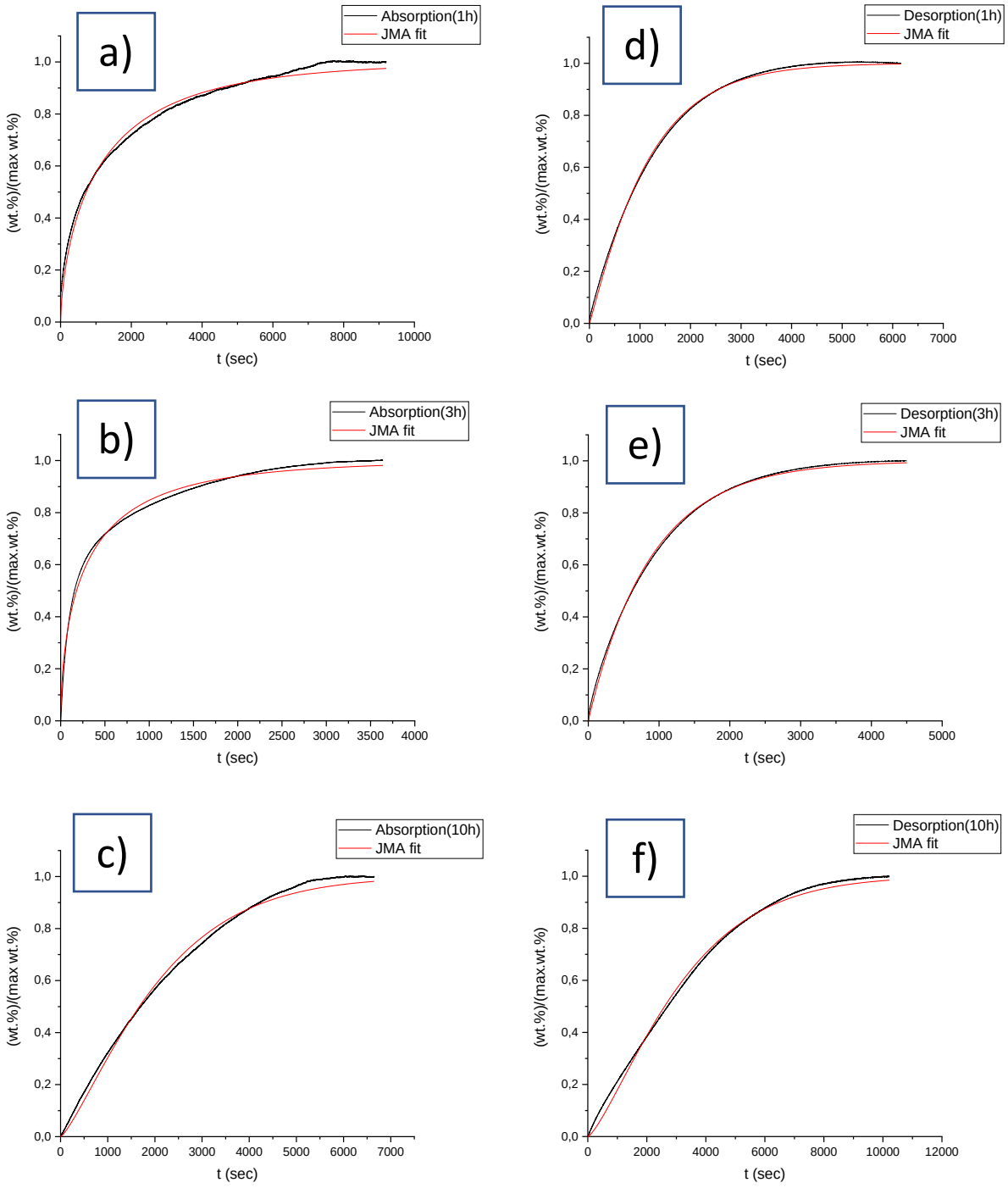

Figure 27. Absorption (a, b, c) and desorption (d, e, f) cycles for MgH_2/FeTi with corresponding JMA fits

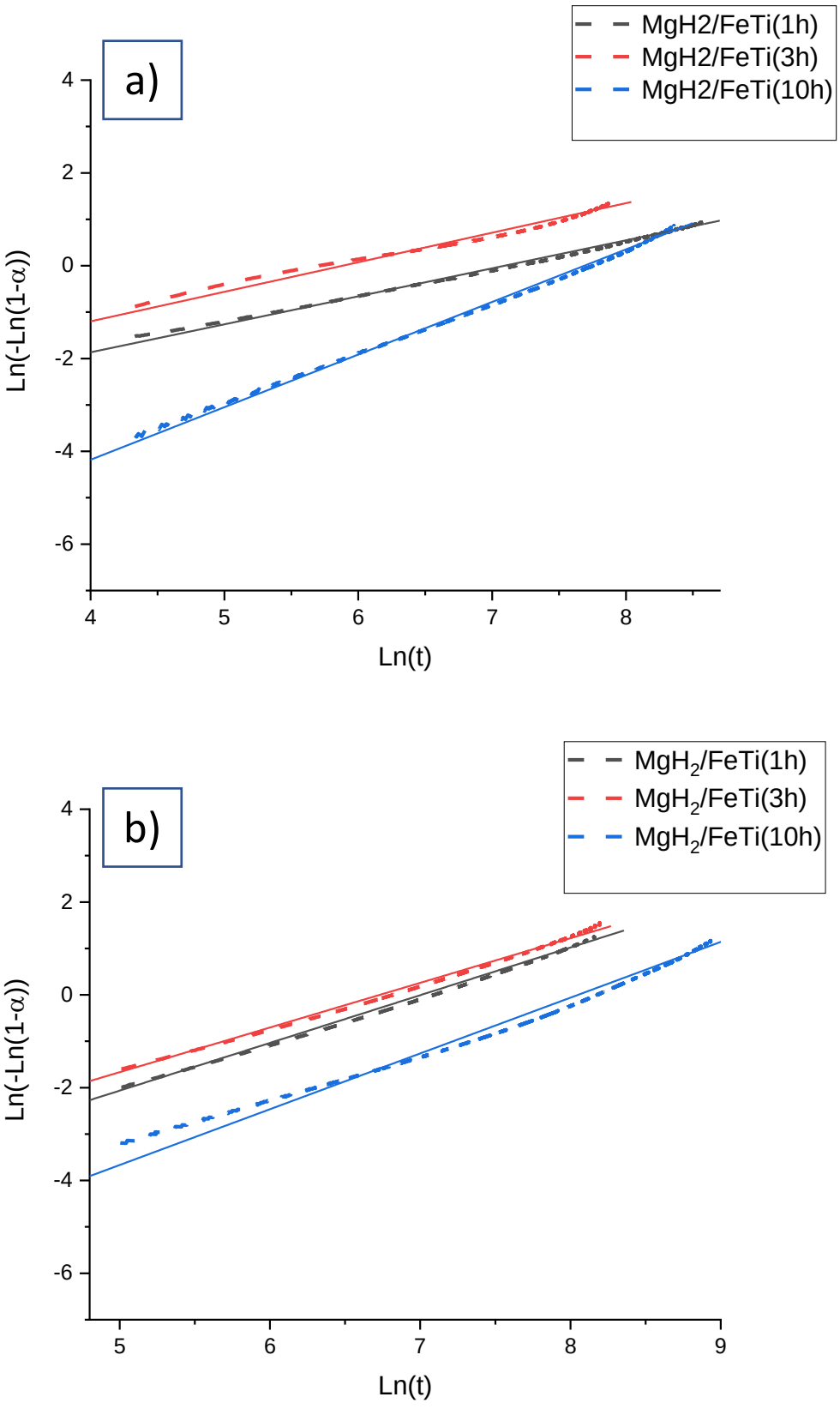

Figure 28. Logarithmic JMA fits against Ln(t) for MgH_2/FeTi Absorption (a) and desorption (b) cycles

As it can be seen from Table 7, the n parameter describing absorption and desorption for the MgH_2/FeTi(1h) and MgH_2/FeTi(3h) samples shows remarkable similarities, however those n values are significantly lower than the usual values obtained for JMA type transformations. According to the thorough review of J.W. Christian these kinetics can be interpreted as a specific type of diffusion-controlled phase growth when precipitate of the new phase (MgH_2 for absorption and Mg for desorption) particles form near lattice defects (vacancies and dislocation lines) [97]. These anomalously low n values correspond to a non-zero slope at t = 0 of the original hydrogenation and dehydrogenation curves (see Fig. 27) unlike for typical JMA functions when the tangent is zero at the beginning of the process. Nevertheless, the n value for the MgH_2/FeTi(10h) powder is definitely larger (2.37 for absorption and 1.32 for desorption) which corresponds to a different sorption mechanism. In our opinion, this mechanism incorporates several distinct processes, such as diffusion-controlled growth with decreasing nucleation rate and nucleation in the vicinity of lattice defects [97].

Table 7. JMA fitting results

Sample	JMA absorption reaction constant [k] (s^{-1})	JMA absorption exponent [n]	JMA desorption reaction constant [k] (s^{-1})	JMA desorption exponent [n]
MgH_2/FeTi(1h)	7.90E-4	0.66	8.52E-4	1.08
MgH_2/FeTi(3h)	29.60E-4	0.58	11.20E-4	0.98
MgH_2/FeTi(10h)	89.00E-4	2.37	2.91E-4	1.32

Conclusions

MgH_2 powder samples catalysed by 10 wt.% of pre-milled FeTi(10h) were obtained by the HEBM with different milling time intervals, 1h, 3h and 10h. The average particle size obtained from SEM experiment was found to be around 2 μm for all powders.

XRD analysis revealed that the milled catalyst predominantly contains $Fe_{0.975}Ti_{0.025}$ solid solution with minor hints of the Fe_2Ti intermetallic compound for the FeTi(10h) mixture. The catalysed MgH_2/FeTi powders are composed of two hydrogen containing phases, α tetragonal and γ high pressure orthorhombic MgH_2. According to Williamson-Hall analysis, average crystallite size is the order of 10 nm for all MgH_2/FeTi samples.

Calorimetry investigations revealed two step dehydrogenation for all milled powders which correspond to the dehydrogenation of γ and α phases at temperatures T1 and T2, respectively. The lowest temperatures for T1, T2 and T_{onset} were achieved for MgH_2/FeTi(3h) sample, indicating that there exists an optimal milling time. Complete hydrogen evolution after two heating runs was observed during post-calorimetry XRD measurements.

All MgH_2/FeTi powder samples can uptake a significant amount of hydrogen in a reasonably short time. Outstanding sorption performance was observed for the MgH_2/FeTi(3h) sample, it was able to absorb 5.2 wt.% of hydrogen in 10 minutes, also, this sample was able to absorb 6.9 wt.% of hydrogen in total. Desorption is almost complete for all powders. JMA model was satisfactory applied to all MgH_2/FeTi normalized sorption curves. n values appeared to be significantly lower than the usual values obtained for JMA type transformations. For the MgH_2/FeTi(1h) and MgH_2/FeTi(3h) samples kinetics can be interpreted as a specific type of diffusion-controlled phase growth when precipitate of the new phase particles forms near lattice defects.

Acknowledgements

I would like to express sincere gratitude to my supervisor Ádám Révész for his scrupulous mentorship and productive support.

Special gratitude should be given to Marcell Gajdics for assistance in performing of ball milling, Péter Nagy for assistance in performing of XRD measurements, Viktória Kovács Kis for performing TEM measurements, Máté Hegedüs for preforming SEM measurements and Tony Spassov for conducting sorption experiment.

References

1. **Schlapbach, L.** Hydrogen as a Fuel and Its Storage for Mobility and Transport. *MRS Bulletin.* 2002, Vol. 27, pp. 675–679.

2. **J. Abe, P. Popoola, E. Ajenifuja, O. Popoola.** Hydrogen energy, economy and storage: Review and recommendation. *International Journal of Hydrogen Energy.* 2019, Vol. 44, pp. 15072–15086.

3. **L. Schlapbach, A. Züttel.** Hydrogen-storage materials for mobile applications. *Nature.* 2001, Vol. 414, pp. 353-358.

4. **R. Krishna, E. Titus, M. Salimian, O. Okhay, S. Rajendran, A. Rajkumar, J. M. G. Sousa, A. L. C. Ferreira, J. C. Gil, J. Gracio.** Hydrogen Storage for Energy Application. [ed.] J. Liu. *Hydrogen Storage.* s.l. : IntechOpen, 2012, p. 280.

5. **Ch. Baerlocher, Lynne B. McCusker, D.H. Olson.** *Atlas of Zeolite Framework Types.* s.l. : Elsevier Science, 2007. p. 404.

6. **J. Dong, X. Wang, H. Xu, Q. Zhao, J. Li.** Hydrogen storage in several microporous zeolites. *International Journal of Hydrogen Energy.* 2007, Vol. 32, pp. 4998–5004.

7. **L. Regli, A. Zecchina, J. G. Vitillo, D. Cocina, G. Spoto, C. Lamberti, K. P. Lillerud, U. Olsbyeb, S. Bordigaa.** Hydrogen storage in Chabazite zeolite frameworks. *Physical Chemistry Chemical Physics.* 2005, Vol. 7, pp. 3197-3203.

8. **Chung, K-H.** High-pressure hydrogen storage on microporous zeolites with varying. *Energy.* 2010, Vol. 35, pp. 2235-2241.

9. **J. Weitkamp, M. Fritz, S. Ernst.** Zeolites as media for hydrogen storage. *International Journal of Hydrogen Energy.* 1995, Vol. 20, 12, pp. 967-970.

10. **V. V. Butova, M. A. Soldatov, A. A. Guda, K. A. Lomachenko, C. Lamberti.** Metal-organic frameworks: structure, properties, methods of synthesis, and characterization. *Russian Chemical Reviews.* 2016, Vol. 85, 3, pp. 280-307.

11. **M. O'Keeffea, M. Eddaoudib, H. Lia, T. Reinekeb, O. M. Yaghib.** Frameworks for Extended Solids: Geometrical Design Principles. *Journal of Solid State Chemistry.* 2000, Vol. 152, 1, pp. 3-20.

12. **Thomas, K. M.** Adsorption and desorption of hydrogen on metal-organic framework materials for storage applications: Comparison with other nanoporous materials. *Dalton Transactions.* 2009, Vol. 9, 9, pp. 1487-1505.

13. **D. Yuan, D. Zhao, D. Sun, H.-C. Zhou.** An Isoreticular Series of Metal–Organic Frameworks with Dendritic Hexacarboxylate Ligands and Exceptionally High Gas-Uptake Capacity. *Angewandte chemie.* 2010, Vol. 49, 31, pp. 5357-5361.

14. **E. Klontzas, E. Tylianakis, G. E. Froudakis.** Hydrogen Storage in 3D Covalent Organic Frameworks. A Multiscale Theoretical. *The Journal of Physical Chemistry C.* 2008, Vol. 112, pp. 9095–9098.

15. **J. L. Mendoza-Cortés, S. S. Han, W. A. Goddard.** High H2 Uptake in Li-, Na-, K-Metalated Covalent Organic Frameworks. *The Journal of Physical Chemistry A.* 2012, Vol. 116, pp. 1621–1631.

16. **H. M. El-Kaderi, J. R. Hunt, J. L. Mendoza-Cortés, A. P. Côté, R.E Taylor, M. O'Keeffe, O. M. Yaghi.** Designed synthesis of 3D covalent organic frameworks. *Science.* 2007, Vol. 13, 316 (5822), pp. 268-272.

17. **S. H. Barghi, T. T. Tsotsis, M. Sahimi.** Chemisorption, physisorption and hysteresis during hydrogen storage in carbonnanotubes. *International Journal of Hydrogen Energy.* 2014, Vol. 39, 3, p. 1390−1397.

18. **H. Kajiura, S. Tsutsui, K. Kadono, M. Kakuta, M. Ata, Y. Murakami.** Hydrogen storage capacity of commercially available carbon materials at room temperature. *Applied Physics Letters.* 2003, Vol. 82, 7, p. 1105−1107.

19. **M. Hirscher, M. Becher, M. Haluska, A. Quintel, V. Skakalova, Y. M. Choi, U. Dettlaff-Weglikowska, S. Roth, I. Stepanek, P. Bernier, A. Leonhardt, J. Fink.** Hydrogen storage in carbon nanostructures. *Journal of Alloys and Compounds.* 2002, Vol. 330, p. 654−658.

20. **B. P. Tarasov, J. P. Maehlen, M. V. Lototsky, V. E. Muradyan, V. A. Yartys.** Hydrogen sorption properties of arc generated single wall carbon nanotubes. *Journal of Alloys and Compounds.* 2003, Vol. 356, p. 510−551.

21. **Z. Y. Tian, Y. T. Liu, W. W. Wu, L. N. Jiang, S. L. Dong.** Hydrogen storage of capped single-walled carbon nanotube via transition-metal doping. *Europhysics Letters.* 2013, Vol. 104, 3, p. 36002.

22. **E. Anikina, A. Banerjee, V. Beskachko, R. Ahuja.** Li-Functionalized Carbon Nanotubes for Hydrogen Storage: Importance of Size Effects. *ACS Applied Nano Materials.* 2019, Vol. 2, p. 3021−3030.

23. **N. A. A. Rusman, M. A. Dahari.** Review on the Current Progress of Metal Hydrides Material for Solid-State Hydrogen Storage Applications. *International Journal of Hydrogen Energy.* 2016, Vol. 41, pp. 12108–12126.

24. **Á. Révész, M. Gajdics.** Improved H-Storage Performance of Novel Mg-Based Nanocomposites Prepared by High-Energy Ball Milling: A Review. *Energies 2021, 14, 6400. https://doi.org/10.3390/en14196400.* 2021, Vol. 14, p. 6400.

25. **Meng, L.** *Improved hydrogen sorption kinetics in wet ball milled Mg hydrides.* s.l. : Forschungszentrum Jülich GmbH, 2011. Schriften des Forschungszentrums Jülich.

26. **Walker, G., [ed.].** *Solid-State Hydrogen Storage.* s.l. : Woodhead Publishing, 2008.

27. **M. H. Mintz, Y. Zeeri.** Hydriding kinetics of powders. *Journal of Alloys and Compounds.* 1994, Vol. 216, 2, pp. 159-175.

28. **Avrami, M.** Kinetics of Phase Change. I General Theory. *Journal of Chemical Physics.* 1939, Vol. 7, 12, pp. 1103-1112.

29. **G. Barkhordarian, T. Klassen, R. Bormann.** Kinetic investigation of the effect of milling time on the hydrogen sorption reaction of magnesium catalyzed with different Nb2O5 contents. *Journal of Alloys and Compounds.* 2006, Vol. 407, 1-2, pp. 249-255.

30. **D., Fátay.** *Hydrogen storage in Mg-based alloys.* Budapest : Eötvös Loránd University, 2010.

31. **A. Züttel, P. Wenger, S. Rentsch, P. Sudan, Ph. Mauron, Ch. Emmenegger.** LiBH4 a new hydrogen storage material. *Journal of Power Sources.* 2003, Vol. 118, 1-2, pp. 1-7.

32. **B. Bogdanović, M. Felderhoff, G. Streukens.** Hydrogen storage in complex metal hydrides. *Journal of the Serbian Chemical Society.* 2009, Vol. 74, 2, pp. 183-196.

33. **G. Barkhordarian, T. Klassen, M. Dornheim, R. Bormann.** Unexpected kinetic effect of MgB2 in reactive hydride composites containing complex borohydrides. *Journal of Alloys and Compounds.* 2007, Vol. 440, 1-2, pp. L18-L21.

34. **N. C. Smythe, J. C. Gordon.** Ammonia Borane as a Hydrogen Carrier: Dehydrogenation and Regeneration. *European Journal of Inorganic Chemistry.* 2010, Vol. 2010, 4, pp. 509-521.

35. **H. T. Hwang, A. Al-Kukhun, A. Varma.** Hydrogen for Vehicle Applications from Hydrothermolysis of Ammonia Borane: Hydrogen Yield, Thermal Characteristics, and Ammonia Formation. *Industrial & Engineering Chemistry Research.* 2010, Vol. 49, 21, pp. 10994–11000.

36. **X-D. Kang, J-H. Luo, P. Wang .** Efficient and highly rapid hydrogen release from ball-milled 3NH3BH3/MMgH3 (M = Na, K, Rb) mixtures at low temperatures. *International Journal of Hydrogen Energy.* 2012, Vol. 37, 5, pp. 4259-4266.

37. **T. B. Lee, M. L. McKee.** Mechanistic Study of LiNH2BH3 Formation from (LiH)4 + NH3BH3 and Subsequent Dehydrogenation. *Inorganic Chemistry.* 2009, Vol. 48, 16, pp. 7564-7575.

38. **H. Pan, Y. Liu, M. Gao, Y. Zhu, Y. Lei.** The structural and electrochemical properties of La0.7Mg0.3(Ni0.85Co0.15)(x) (x=3.0-5.0) hydrogen storage alloys. *International Journal of Hydrogen Energy.* 2003, Vol. 28, 11, pp. 1219-1228.

39. **J. Prigent, J.-M. Joubert, M. Gupta.** Modification of the hydrogenation properties of LaNi5 upon Ni substitution by Rh, Ir, Pt or Au. *Journal of Alloys and Compounds.* 2012, Vol. 511, 1, pp. 95-100.

40. **M. C. Georgiadis, E. S. Kikkinides, S. S. Makridis, K. Kouramas, E. N. Pistikopoulos.** Design and optimization of advanced materials and processes for efficient hydrogen storage. *Computers and Chemical Engineering.* 2009, Vol. 33, 5, pp. 1077-1090.

41. **K. D. Ćirića, A. Kocjan, A. Gradišek, V. J. Koteski, A. M. Kalijadis, V. N. Ivanovski, Z. V. Laušević, D. Lj. Stojić.** A study on crystal structure, bonding and hydriding properties of Ti–Fe–Ni intermetallics – Behind substitution of iron by nickel. *International Journal of Hydrogen Energy.* 2012, Vol. 37, 10, pp. 8408-8417.

42. **F. Cuevas, M. Latroche, A. Percheron-Guegan.** Relationship between polymorphism and hydrogenation properties in Ti0.64Zr0.36Ni alloy. *Journal of Alloys and Compounds.* 2005, Vols. 404-406, pp. 545-549.

43. **Orgaz, E.** The electronic structure of the Laves phase intermetallics LnM2 (Ln=Y, La–Lu, M=Mg, Al) and the LaMg2H7 and CeMg2H7 hydrides. *Journal of Alloys and Compounds.* 2001, Vol. 322, 1-2, pp. 45-54.

44. **S. Mitrokhin, T. Zotov, E. Movlaev, V. Verbetsky.** Hydrogen interaction with intermetallic compounds and alloys at high pressure. *Journal of Alloys and Compounds.* 2013, Vol. 580, pp. S90–S93.

45. **K. Young, B. Reichman, M. A. Fetcenko.** Electrochemical performance of AB2 metal hydride alloys measured at −40°C. *Journal of Alloys and Compounds 580.* 2013, Vol. 580, pp. S349-S352.

46. **V. A. Yartys, M. V. Lototskyy, E. Akiba, R. Albert, V. E. Antonov, J. R. Ares, M. Baricco, N. Bourgeois et al.** Magnesium based materials for hydrogen based energy storage: Past, present and future. *International Journal of Hydrogen Energy.* 2019, Vol. 44, 15, pp. 7809-7859.

47. **K. Zeng, T. Klassen, W. Oelerich R. Bormann.** Critical Assessment and Thermodynamic Modeling of the Mg–H System. *International Journal of Hydrogen Energy.* 1999, Vol. 24, pp. 989–1004.

48. **R. A. Varin, T. Czujko, Z. S. Wronski.** *Nanomaterials for Solid State Hydrogen Storage.* Boston : Springer, 2009. p. 338.

49. **T. Noritake, M. Aoki, S. Towata, Y. Seno, Y. Hirose, E. Nishibori, M. Takata, M. Sakata.** Chemical bonding of hydrogen in MgH2. *Applied Physics Letters 81.* 2002, Vol. 81, 11, p. 2008.

50. **J. C. Crivello, B. Dam, R. V. Denys, M. Dornheim, D. M. Grant, J. Huot, T. R. Jensen, P. de Jongh, M. Latroche, C. Milanese.** Review of magnesium hydride-based materials: development and optimisation. *Applied Physics A: materials science & processing.* 2016, Vol. 122, 2, pp. 1-20.

51. **J. F. Fernández, C. R. Sánchez.** Rate determining step in the absorption and desorption of hydrogen by magnesium. *Journal of Alloys and Compounds.* 2002, Vol. 340, 1-2, pp. 189-198.

52. **L. Zaluski, A. Zaluska, P. Tessier, J. O. Stroem-Olsen, R. Schulz.** Nanocrystalline Hydrogen Absorbing Alloys. *Material Science Forum.* 1996, Vols. 225-227, pp. 853-858.

53. **W. Oelerich, T. Klassen, R. Bormann.** Metal oxides as catalysts for improved hydrogen sorption in Nanocrystalline Mg-based materials. *Journal of Alloys and Compounds.* 2001, Vol. 315, pp. 237–242.

54. **Pasquini, L.** The Effects of Nanostructure on the Hydrogen Sorption Properties of Magnesium-Based Metallic Compounds: A Review. *Crystals.* 2018, Vol. 8, p. 106.

55. **D. Fátay, T. Spassov, P. Delchev, G. Ribárik G, Á. Révész.** Microstructural development in nanocrystalline MgH2 during H-absorption/desorption cycling. *International Journal of Hydrogen Energy.* 2007, Vol. 32, pp. 2914-2919.

56. **Á. Révész, D. Fátay.** Microstructural evolution of ball-milled MgH2 during a completedehydrogenation-hydrogenation cycle. *Journal of Power Sources.* 2010, Vol. 195, pp. :6997-7002.

57. **G. Urretavizcaya, G. García, D. Serafini, G. Meyer.** Mg-Ni alloys for hydrogen storage obtained by ball milling. *Latin American Applied Research.* 2002, Vol. 32, pp. 289–294.

58. **Á. Révész, M. Gajdics, T. Spassov.** Microstructural evolution of ball-milled Mg–Ni powder during hydrogen sorption. *International Journal of Hydrogen Energy.* 2013, Vol. 38, pp. 8342–8349.

59. **M. Polanski, J. Bystrzycki, T. Plocinski.** The effect of milling conditions on microstructure and hydrogen absorption/desorption properties of magnesium hydride (MgH2) without and with Cr2O3 nanoparticles. *International Journal of Hydrogen Energy.* 2008, Vol. 33, pp. 1859-1867.

60. **J. G. Novakovic, N. Novakovic, S. Kurko, S. M. Govedarovic, T. Pantic, B. P. Mamula, et al.** Influence of defects on the stability and hydrogen-sorption behavior of Mg-based hydrides. *ChemPhysChem.* 2019, Vol. 20, pp. 1216–1247.

61. **X. Yao, Z.H. Zhu, H.M. Cheng, G.Q. Lu.** Hydrogen diffusion and effect of grain size on hydrogenation kinetics in magnesium hydrides. Materials Research Society, 2008, Vol. 23, pp. 336-340.

62. **Z. Dehouche, R. Djaozandry, J. Huot, S. Boily.** Influence of cycling on the thermodynamic and structure properties of nanocrystalline magnesium based hydride. Journal of Alloys and Compounds, 2000, Vol. 305, pp. 264–271.

63. **S. Zhou, Q. Zhang, H. Chen, X. Zang, X. Zhou, R. Wang, X. Jiang, B. Yang, R. Jiang.** Crystalline structure, energy calculation and dehydriding thermodynamics of magnesium hydride from reactive milling. *International Journal of Hydrogen Energy.* 2015, Vol. 40, pp. 11484–11490.

64. **Á. Révész, M. Gajdics, E. Schafler, M. Calizzi, L. Pasquini, L.** Dehydrogenation-hydrogenation characteristics of nanocrystalline Mg2Ni powders compacted by high-pressure torsion. *Journal of Alloys and Compounds.* 2017, Vol. 702, pp. 84–91.

65. **D. Khan, J. Zou, X. Zeng, W. Ding.** Hydrogen storage properties of nanocrystalline Mg2Ni prepared from compressed 2MgH2–Ni powder. *International Journal of Hydrogen Energy.* 2018, Vol. 43, 49, pp. 22391–22400.

66. **S. D. House, J. J. Vajo, C. Ren, N. J. Zaluzec, A. A. Rockett, I. M. Robertson.** Impact of Initial Catalyst Form on the 3D Structure and Performance of Ball-Milled Ni-Catalyzed MgH2 for Hydrogen Storage. *International Journal of Hydrogen Energy.* 2017, Vol. 42, pp. 5177–5187.

67. **Q. Zhang, L. Zang, Y. Huang, P. Gao, L. Jiao, H. Yuan, Y. Wang.** Improved hydrogen storage properties of MgH2 with Ni-based compounds. *International Journal of Hydrogen Energy.* 2017, Vol. 42, pp. 24247–24255.

68. **S. Kumar, A. Singh, G. P. Tiwari, Y. Kojima, V. Kain .** Thermodynamics and Kinetics of Nano-Engineered Mg-MgH2 System for Reversible Hydrogen Storage Application. *Thermochimica Acta.* 2017, Vol. 652, pp. 103-108.

69. **F. J. Antiqueira, D. R. Leiva, G. Zepon, B. F. R. F. de Cunha, S. J. A. Figueroa, W. J. Botta .** Fast Hydrogen Absorption/Desorption Kinetics in Reactive Milled Mg-8 Mol% Fe Nanocomposites. *International Journal of Hydrogen Energy.* 2020, Vol. 45, pp. 12408–12418.

70. **M. Y. Song, I. H. Kwon, S. N. Kwon, C. G. Park, H. R. Park, J.-S. Bae.** Preparation of hydrogen-storage alloy Mg–10wt% Fe2O3 under various milling conditions. *Internation Journal of Hydrogen Energy.* 2006, Vol. 31, pp. 43-47.

71. **M. Y. Song, Y. J. Kwak .** Hydrogen Charging Kinetics of Mg - 10wt% Fe2O3 Prepared via MgH2-Forming Mechanical Milling. *Materials Research Bulletin.* 2021, Vol. 140, p. 111304.

72. **Y. Sun, C. Shen, Q. Lai, W. Liu, D.-W. Wang, K.-F. Aguey-Zinsou.** Tailoring Magnesium Based Materials for Hydrogen Storage through Synthesis: Current State of the Art. *Energy Storage Materials.* 2018, Vol. 10, pp. 168–198.

73. **Z. Ma, J. Liu, Y. Zhu, Y. Zhao, H. Lin, Y. Zhang, H. Li, J. Zhang, Y. Liu, W. Gao et al.** Crystal-Facet-Dependent Catalysis of Anatase TiO2 on Hydrogen Storage of MgH2. *Journal of Alloys and Compounds.* 2020, Vol. 822, p. 153553.

74. **M. Zhang, X. Xiao, X. Wang, M. Chen, Y. Lu, M. Liu, L. Chen.** Excellent Catalysis of TiO2 Nanosheets with High-Surface-Energy {001} Facets on the Hydrogen Storage Properties of MgH2. *Nanoscale.* 2019, Vol. 11, pp. 7465–7473.

75. **R. A. Silva, R. M. Leal Neto, D. R. Leiva, T. T. Ishikawa, C. S. Kiminami, A. M. Jorge, W. J. Botta.** Room Temperature Hydrogen Absorption by Mg and MgTiFe Nanocomposites Processed by High-Energy Ball Milling. *International Journal of Hydrogen Energy.* 2018, Vol. 43, pp. 12251–12259.

76. **R. M. L. Neto, R. de Araújo Silva, R. Floriano, G. C. S. Coutinho, R. B. Falcão, D. R. Leiva, W. J. Botta Filho.** Synthesis by High-Energy Ball Milling of MgH2-TiFe Composites for Hydrogen Storage. *Materials Science Forum.* 2017, Vol. 899, pp. 13-18.

77. **M. S. El-Eskandarany, E. Shaban, F. Aldakheel, A. Alkandary, M. Behbehani, M. Al-Saidi.** Synthetic Nanocomposite MgH2/5wt.% TiMn2 Powders for Solid-Hydrogen Storage Tank Integrated with PEM Fuel Cell. *Scientific Reports.* 2017, Vol. 7, p. 13296.

78. **M. S. El-Eskandarany, E. Shaban, H. Al-Matrouk, M. Behbehani, A. Alkandary, F. Aldakheel, N. Ali, S. A. Ahmed.** Structure, Morphology and Hydrogen Storage Kinetics of Nanocomposite MgH2/10wt% ZrNi5 Powders. *Materials Today Energy.* 2017, Vol. 3, pp. 60-71.

79. **El-Eskandarany, M. S.** Metallic Glassy Ti2Ni Grain-Growth Inhibitor Powder for Enhancing the Hydrogenation/Dehydrogenation Kinetics of MgH2. *RSC Advances.* 2019, Vol. 9, pp. 1036–1046.

80. **M. S. El-Eskandarany, M. Saeed, E. Al-Nasrallah, F. Al-Ajmi, M. Banyan.** Effect of LaNi3 Amorphous Alloy Nanopowders on the Performance and Hydrogen Storage Properties of MgH2. *Energies.* 2019, Vol. 12, p. 1005.

81. **J. Zhang, R. Shi, Y. Zhu, Y. Liu, Y. Zhang, S. Li, L. Li.** Remarkable Synergistic Catalysis of Ni-Doped Ultrafine TiO2 on Hydrogen Sorption Kinetics of MgH2. *ACS Applied Materials & Interfaces.* 2018, Vol. 10, pp. 24975–24980.

82. **M. Chen, X. Xiao, M. Zhang, J. Zheng, M. Liu, X. Wang, L. Jiang, L. Chen.** Highly Dispersed Metal Nanoparticles on TiO2 Acted as Nano Redox Reactor and Its Synergistic Catalysis on the Hydrogen Storage Properties of Magnesium Hydride. *International Journal of Hydrogen Energy.* 2019, Vol. 44, pp. 15100–15109.

83. **H. Gao, R. Shi, J. Zhu, Y. Liu, Y. Shao, Y. Zhu, J. Zhang, L. Li, X; Hu.** Interface Effect in Sandwich like Ni/Ti3C2 Catalysts on Hydrogen Storage Performance of MgH2. *Applied Surface Science.* 2021, Vol. 564, p. 150302.

84. **K. Wang, G. Wu, H. Cao, H. Li, X. Zhao.** Improved Reversible Dehydrogenation Properties of MgH2 by the Synergetic Effects of Graphene Oxide-Based Porous Carbon and TiCl3. *International Journal of Hydrogen Energy.* 2018, Vol. 43, pp. 7440–7446.

85. **K. Wang, X. Zhang, Y. Liu, Z. Ren, X. Zhang, J. Hu, M. Gao, H. Pan.** Graphene-Induced Growth of N-Doped Niobium Pentaoxide Nanorods with High Catalytic Activity for Hydrogen Storage in MgH2. *Chemical Engineering Journal.* 2021, Vol. 406, p. 126831.

86. **X. Huang, X. Xiao, W. Zhang, X. Fan, L. Zhang, C. Cheng, S. Li, H. Ge, Q. Wang, L. Chen.** Transition metal (Co, Ni) nanoparticles wrapped with carbon and their superior catalytic activities for the reversible hydrogen storage of magnesium hydride. *Physical Chemistry Chemical Physics.* 2017, Vol. 19, pp. 4019–4029.

87. **H. Yong, X. Wei, J. Hu, Z. Yuan, S. Guo, D. Zhao, Y. Zhang.** Hydrogen Storage Behavior of Mg-Based Alloy Catalyzed by Carbon-Cobalt Composites. *Journal of Magnesium and Alloys.* 2021, Vol. 9, pp. 1977-1988.

88. **X. Hou, R. Hu, T. Zhang, H. Kou, J. Li.** Hydrogenation Thermodynamics of Melt-Spun Magnesium Rich Mg–Ni Nanocrystalline Alloys with the Addition of Multiwalled Carbon Nanotubes and TiF3. *Journal of Power Sources.* 2016, Vol. 306, pp. 437–447.

89. **M. Gajdics, T. Spassov, V. Kovács Kis, E. Schafler, Á. Révész.** Microstructural and morphological investigations on Mg-Nb2O5-CNT nanocomposites processed by high-pressure torsion for hydrogen storage applications. *International Journal of Hydrogen Energy.* 2020, Vol. 45, pp. 7917-7928.

90. **Y.-S. Chuang, S.-J. Hwang.** Synthesis and Hydrogen Absorption/Desorption Properties of Mg–Nb2O5–SWCNT/MWCNT Nanocomposite Prepared by Reactive Milling. *Journal of Alloys and Compounds.* 2016, Vol. 656, pp. 835–842.

91. **R. Vijay, R. Sundaresan, M.P. Maiya, S. Srinivasa Murthy, Y. Fu, H.-P. Klein, M. Groll.** Characterisation of Mg–x wt.% FeTi (x = 5–30) and Mg–40 wt.% FeTiMn hydrogen absorbing materials prepared by mechanical alloying. *Journal of Alloys and Compounds.* 2004, Vol. 384, pp. 283-295.

92. **Suryanarayana, C.** Mechanical alloying and milling. *Progress in Materials Science.* 2001, Vol. 46, 1-2, pp. 1–184.

93. **Urakaev, F. K. H.** 2—Mechanism and kinetics of mechanochemical processes. [ed.] M. Sopicka-Lizer. *High-Energy Ball Milling.* Sawston, UK : Woodhead Publishing, 2010, pp. 9–44.

94. **A. Zolriasatein, A. Shokuhfar, F. Safari, N. Abdi.** Comparative study of SPEX and planetary milling methods for the fabrication of complex metallic alloy nanoparticles. *Micro & Nano Letters.* 2018, Vol. 13, pp. 448–451.

95. **Révész, Á.** *Microstructure and Thermal Properties of Nanocrystalline Materials.* Budapest, Hungary : Eötvös University, 2000. Ph.D. Thesis.

96. **Révész Á., Dániel G. Fodor, Krállics G., Spassov T., and Gajdics M.** Structural and hydrogen storage characterization of nanocrystalline magnesium synthesized by ECAP and catalyzed by different nanotube additives. *Reviews on Advanced Materials Science*. 2021, Vol. 60, pp. 1–10

97. **J.W. Christian.** The Theory of Transformations in Metals and Alloys. *PERGAMON*. Oxford, 1975, pp. 534-542.